Phase equilibria in the Fe-Mo-Ti ternary system at 1000°C

A.J. Knowles[1], N.G. Jones[1], O.M.D.M. Messé[1], J.S. Barnard[1], C.N. Jones[2], H.J. Stone[1]

1 - Department of Materials Science and Metallurgy, University of Cambridge, 27 Charles Babbage Road, Cambridge CB3 0FS, UK
2 - Rolls-Royce plc, P.O. Box 31, Derby, DE24 8BJ, UK

Keywords
Phase stability; Molybdenum alloys; Titanium alloys; Microstructure; Electron microscopy, scanning; Electron microscopy, transmission

Abstract

An isothermal section of the Fe-Mo-Ti ternary system at 1000°C has been constructed using data acquired from a series of seven alloys. The limit of solubility of Fe in the continuous A2 phase field between Ti and Mo has been determined, as have the extents to which Mo may be accommodated in the B2 TiFe phase, and Ti in the $D8_5$ Fe_7Mo_6 phase. The B2, $D8_5$ and C14 Fe_2Ti intermetallics were found to have limited tolerance for non-stoichiometric compositions. The positions of the A2+B2+C14 and A2+C14+$D8_5$ three-phase fields were determined, along with the extents of the A2+B2, A2+$D8_5$, A2+C14, C14+B2 and C14+$D8_5$ two-phase fields. No ternary phases were observed in any of the alloys studied.

1.0 Introduction

Eutectic alloys with two-phase microstructures based on an A2† Ti solid solution and a B2† TiFe intermetallic phase have been shown to possess strengths up to 2.5 GPa and elongations to failure of 15% [1,2]. These properties have led to the suggestion that such materials have potential for high strength structural applications. The effect of ternary additions (Nb, V and Sn) on the microstructure and properties of these alloys have been studied and shown to promote microstructural refinement, alter the lattice misfit, and improve both strength and strain to failure [3-5]. However, to date, no assessment has been made of the effect of Mo additions on the properties of such alloys, despite it offering several potential benefits. Mo is a potent stabiliser of the A2 phase in Ti, suppressing the allotropic transformation to the A3 phase. In addition, complete miscibility exists between A2 Ti and A2 Mo at elevated temperatures [6], whilst only modest concentrations of Mo can be accommodated in B2 TiFe [7]. This differential solubility offers the possibility of tailoring the lattice misfit between the A2 and B2 phases, modifying the interfacial coherency, as well as providing additional solid solution strengthening.

Many studies have considered the phase equilibria in the Fe-Mo-Ti ternary system [7-14]. However, there have been only limited experimental studies of isothermal sections in the system [13,14], which have been used to instruct thermodynamic assessments [8,14]. Critically, inconsistencies exist between these sections and the corresponding phase boundaries reported in the associated binary systems. An overview of the three constituent binary phase diagrams is presented in Figure 1 and includes: the Fe-Ti diagram of Hong *et al*. [15], the Fe-Mo diagram of Rajkumar and Kumar [16], as well as the Mo-Ti diagram of Franke and Neuschütz, [6]. A summary of the phases present in these binary systems, their crystal structures, and compositions, is provided in Table 1. Pure Mo adopts the A2 structure at all temperatures, whilst Ti and Fe exhibit allotropic transformations. Within the Mo-Ti binary system, a continuous A2 phase field exists above 882°C and below the solidus temperature [6,17,18]. However, in the Fe-Ti and Fe-Mo binary systems, intermetallic phases limit the continuity of the A2 phase fields. In the Fe-Ti binary system, the TiFe B2 intermetallic phase is congruently formed and stable from room temperature up to its melting point of 1319°C. Both the Fe-Ti and Fe-Mo binary phase diagrams contain an Fe_2X (X = Ti, Mo) C14 Laves phase, which is stable up to melting at 1433°C in the Fe-Ti system, but unstable above 927°C in the Fe-Mo system. In addition, the Fe-Mo system also contains two other high temperature intermetallics, the R and $D8_b$ σ phases, as well as the $D8_5$ μ phase, which is stable from room temperature to 1370°C.

A key discrepancy between the published binary phase diagrams is whether the intermetallic phases are line compounds, or may tolerate non-stoichiometric compositions. In the Fe-Ti binary system, a number of thermodynamic assessments described TiFe, and also Fe_2Ti, as line compounds [19-21]. This is in disagreement with earlier experimental work, which reported solubility ranges of ~ 2 at.% for TiFe and ~ 5 at.% for Fe_2Ti [22-24]. Similar solubility ranges for both phases have been included in the most recent thermodynamic assessment of this system [15]. Of the intermetallic phases

† Strukurbericht notation

stable at room temperature in the Fe-Mo binary system, the $D8_5$ phase has consistently been reported to have a solubility range of ~ 5 at.%, whilst the C14 Laves phase has been treated as a line compound [16,25,26].

The most complete investigation of the Fe-Mo-Ti ternary system has been that of Jin and Qiu [14], who performed a diffusion couple experiment focussed on the Fe-Ti rich portion of the phase diagram at 1000°C and conducted a thermodynamic assessment with the results obtained. Their isothermal section of this system has been included in the centre of Figure 1. In their study, TiFe was reported as being a line compound. This is in contrast to previous binary [22] and ternary studies [13,27], where this phase has been shown to tolerate non-stoichiometric compositions. Substitution of Mo for Ti in the C14 Laves phase has also been reported at both 1000°C [14] and 900°C [7,9], and its phase field was shown to be continuous across ternary space at 900°C [7,9]. However, the extent to which Fe and Ti may be substituted in this phase is inconsistent between the binary [15] and ternary [14] system assessments. The $D8_5$ Fe_7Mo_6 phase has been reported to accommodate non-stoichiometric compositions of up to ~ 5 at.% between Mo and Fe [14,16]. However, the reported maximum ternary solubility for Ti in this phase varies dramatically, from 14.55 at.% [14] to near zero [13], which highlights the need for new measurements.

Previous studies of the Fe-Mo-Ti ternary system have concentrated on the Fe-rich corner. As such, limited data has been obtained as to the locations of the phase boundaries between the A2 (Ti, Mo) solid solution and the intermetallic compounds. The present paper seeks to address this by determining the locations of the A2+B2+C14 & A2+$D8_5$+C14 three-phase fields and resolve the extents of the A2+B2, A2+$D8_5$ & A2+C14 two-phase regions. Special attention has also been given to determining the solubility of Fe in the A2 phase as the Mo:Ti ratio varies, the solubility of Mo in B2 TiFe and the solubility of Ti in $D8_5$ Fe_7Mo_6.

2.0 Experimental

Seven alloys with compositions within the Ti- and Mo-rich portion of the Fe-Mo-Ti ternary phase diagram were investigated. The nominal compositions of these alloys, in at.%, are given in Table 2. The alloys will subsequently be referred to as TF*x*M*y* in which *x* is the nominal concentration of Fe and *y* is the concentration of Mo in at.%, with the balance being Ti. Alloys were created from elemental metals, with purity ≥ 99.9 % and arc melted under an Ar atmosphere to form cylindrical bars approximately 60 mm in length and 10 mm in diameter. The ingots were inverted and remelted 5 times in order to improve compositional homogeneity. Samples cut from each of the alloys were encapsulated in evacuated and Ar-backfilled quartz ampoules along with pure Ti granules to getter any residual oxygen. The encapsulated samples were heat treated at 1000°C for 500 hours, followed by water quenching.

Microstructural characterisation was performed on samples in both the as-cast and heat-treated conditions. Scanning electron microscopy (SEM) was performed on JEOL 5800 and FEI Nova NanoSEM 450 microscopes. SEM-based energy dispersive X-ray spectroscopy (SEM-EDX) was used to determine compositions, with pure Ti used as a calibration standard. Bulk compositions were determined by averaging five 200 × 400 μm area measurements, at the top, bottom, centre and at either side of each bar. Individual phase compositions were determined from the average of all of the clustered SEM-EDX point measurements. These spectra were acquired in pairs, or triplets, close to the boundaries between adjacent phases, where the material will have been in local equilibrium. The probe diameter was estimated to be ~ 1 μm, whilst the penetration depth was estimated to be ~ 3 μm, using the Kanaya-Okayama relationship [28]. The quoted uncertainty of these compositions was the standard deviation of the data.

Samples for examination using transmission electron microscopy (TEM) were electro-polished using a solution of 10 vol.% perchloric acid in methanol at -30°C and 18 V. Final thinning of the foils was performed using a GATAN precision ion polishing system operated at 5 kV, with the Ar flow rate adjusted to give a current of ~ 15 μA. TEM was carried out using a FEI Tecnai Osiris, capable of scanning transmission electron microscopy (STEM). STEM-based energy dispersive X-ray spectrometry (STEM-EDX) was performed using a Super-X EDX detection system in order to determine phase compositions. STEM-EDX spectra were acquired whilst scanning the nanometre-sized probe over a 500 × 500 nm area within regions of the microstructure coarse enough to sample a single phase. As with the SEM-EDX measurements, the reported phase compositions were obtained by averaging three independent measurements and the quoted uncertainty is their standard deviation.

X-ray diffraction (XRD) was performed using a Bruker D8 θ–2θ diffractometer with a Cu source operated at 40 kV and 40 mA. Diffraction spectra were collected between 20 and 80° 2θ with a step size of 0.03° 2θ and a total collection time of 2 hours. A maximum area of approximately 5 × 5 mm was illuminated and the samples were spun at 30 rpm during data acquisition to minimise textural effects. Analysis of the diffraction data was performed with the TOPAS software using the Pawley method, with the crystallographic data presented in Table 1 as the starting point.

3.0 Results

SEM imaging of the samples in the as-cast state indicated that all the alloys had a dendritic microstructure, as would be expected for arc melted material. The bulk compositions of the alloys, determined by large area SEM-EDX measurements, are given in Table 2 and the values were considered to be in adequate agreement with the nominal compositions. The homogeneity of the alloys was also considered satisfactory, with the standard deviation between measurements made at different locations in each bar being less than 2 at.%.

The following sections discuss the results obtained from each of the seven alloys following heat treatment at 1000°C individually, before the key observations are combined to produce an isothermal section.

3.1 TF20M10

SEM-EDX area analysis on alloy TF20M10 determined it to have a bulk composition of 70.2Ti-19.6Fe-10.2Mo, as shown in Table 2.

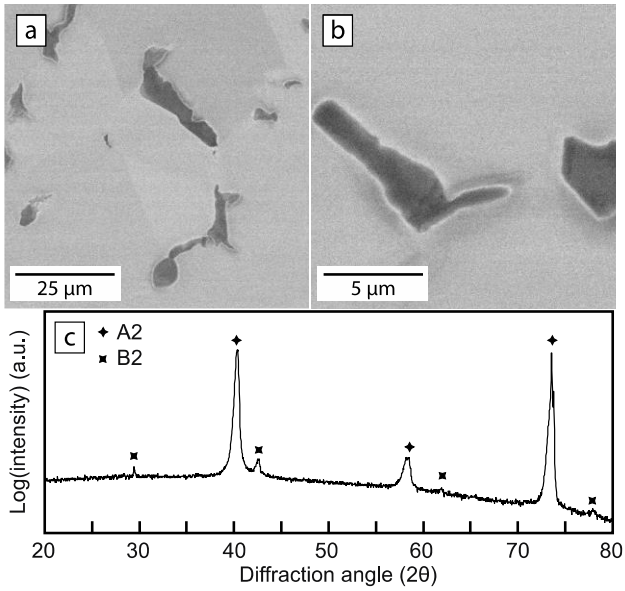

Figure 2**a shows a representative backscattered electron (BSE) micrograph obtained from this alloy after the heat treatment at 1000°C. A two-phase microstructure can be observed, with bright primary dendrites and a darker interdendritic phase, which was present in a significantly lower volume fraction. Imaging at higher magnifications, as shown in**

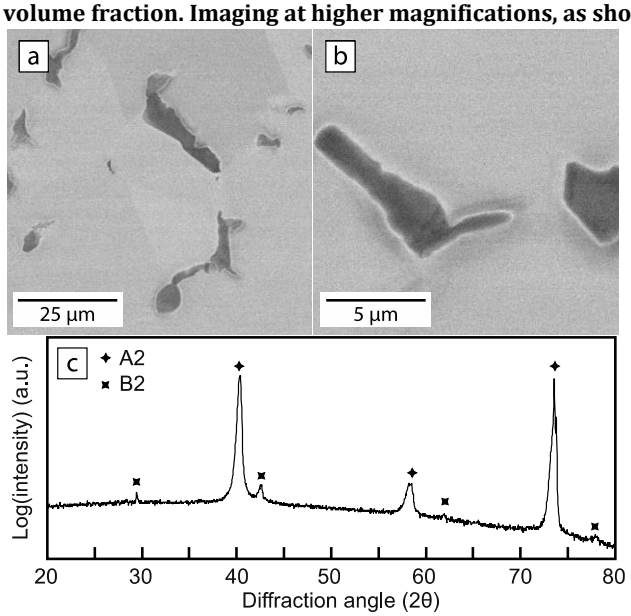

Figure **2**b, did not reveal any additional phases.

The X-ray diffraction spectrum acquired from alloy TF20M10, shown in Figure 2c, contained reflections corresponding to both A2 and B2 phases. The large grain size in the sample prohibited Rietveld refinement of the data. However, comparison of peak areas from the two phases suggested that there was significantly more of the A2 phase in the alloy than the B2 phase. It was therefore deemed likely that the primary bright phase observed in BSE imaging was the A2 phase and the secondary darker phase the B2 phase. Pawley refinement of the diffraction spectrum gave a lattice of a_{A2} = 3.15 ± 0.01 Å for the A2 phase, and a_{B2} = 3.00 ± 0.01 Å for the B2 phase, Table 3. This suggested a lattice misfit between these phases of δ ~ 5%, as defined by δ = (a_{B2}-a_{A2})/a_{A2}.

SEM-EDX analysis indicated that the bright phase had a composition of 71.4±0.2Ti-17.7±0.1Fe-10.8±0.1Mo, whilst the darker B2 phase had a composition of 52.4±0.2Ti-45.7±0.3Fe-1.9±0.1Mo. These compositions are consistent with the A2 and B2 phases in the Ti-Fe binary system, shown in

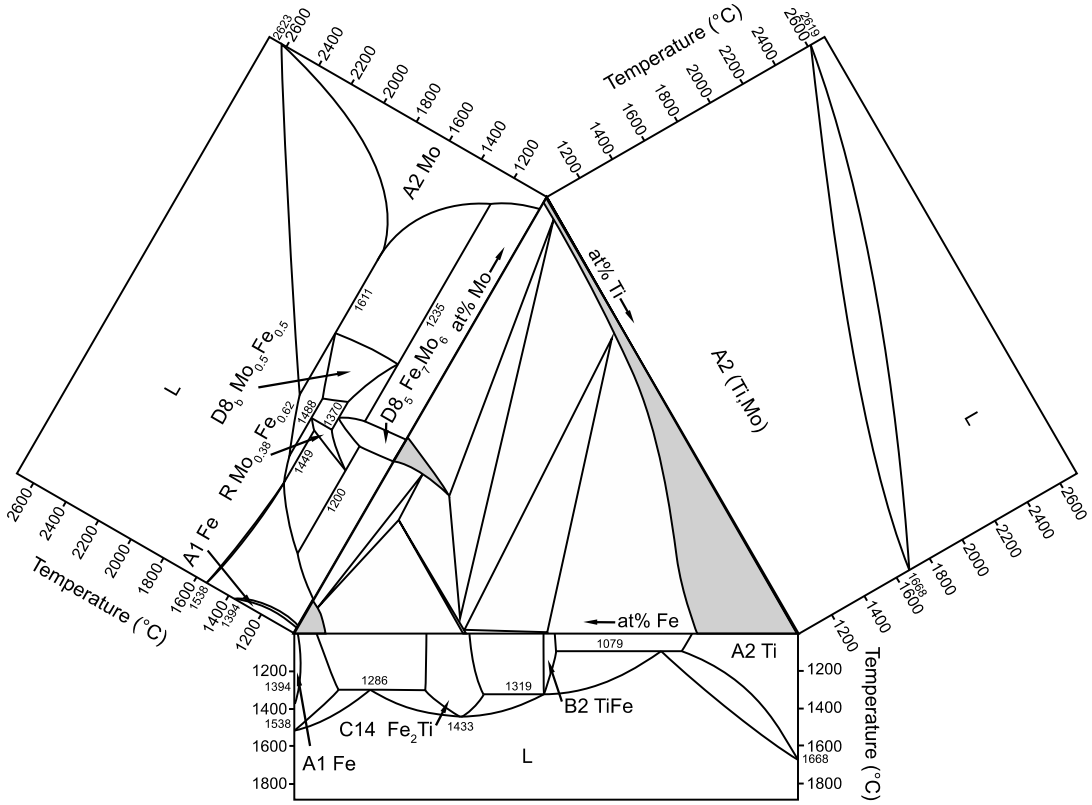

Figure **1** and Table 1, supporting the phase identification by XRD. The large difference in the Mo contents of the two phases accounted for the differential atomic number contrast seen between them using BSE imaging.

Closer examination of A2 diffraction peaks in the XRD spectrum identified the existence of a broader peak at lower diffraction angles than the sharp $K\alpha_1,\alpha_2$ A2 peaks, an example of which is given in

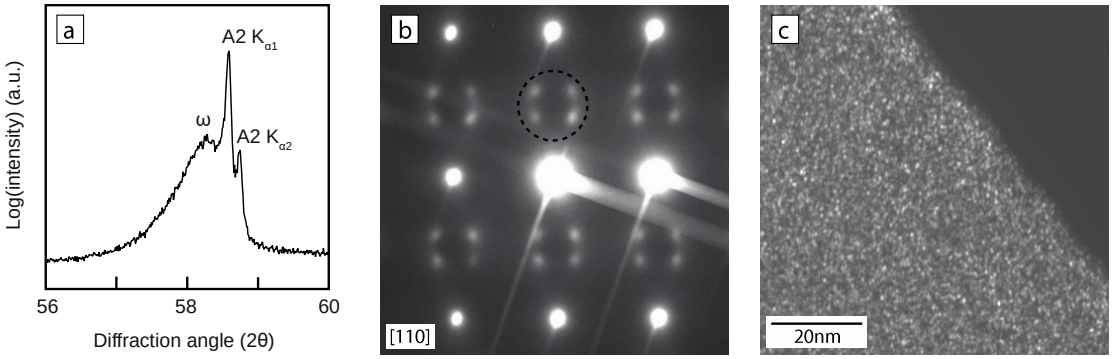

Figure **3**a. The large area of these broad peaks suggested that a third phase, with a substantial volume fraction, was present in the alloy. However, only two phases where identified by SEM imaging. The broad width of these peaks suggested that the third phase may be very fine and so beyond the resolution limit of SEM imaging. To resolve the nature of the third phase, the sample was studied using TEM.

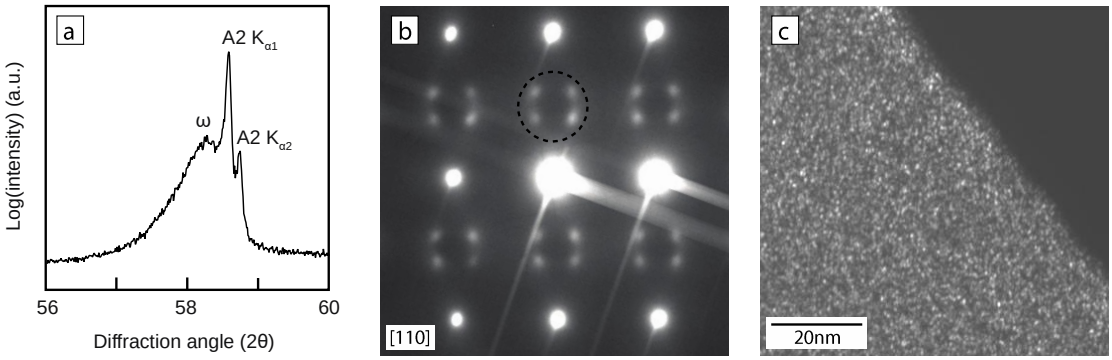

Figure **3**b shows a selected area diffraction pattern (SADP) taken within the A2 phase along a <110>, in which strong A2 diffraction spots may be clearly observed. However, additional reflections were also present, highlighted by the dashed circle. Similar patterns have been reported previously in water quenched Ti – 22% Fe [29] and other commercial alloys [30,31], which have been attributed to the incommensurate omega phase. The dark field (DF) image shown in

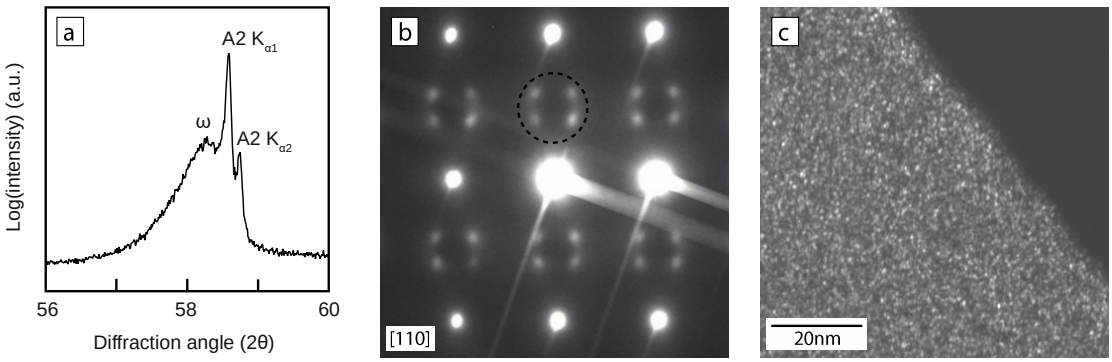

Figure **3**c was formed using the reflections within the dashed circle in Figure 3b. A distribution of exceptionally fine particles (~ 1 nm) was observed, consistent with the broad peaks in the XRD spectrum. Given that the diffusion distances for a 500 hour heat treatment are well over a micron and that athermal omega is known to form on rapid cooling of beta stabilised Ti alloys [29,32,33], it was concluded that the omega phase was not present at 1000°C.

3.2 TF20M20

Alloy TF20M20 had a bulk composition of 58.8Ti-20.0Fe-21.2Mo, as determined by large area SEM-EDX analysis. BSE imaging identified two phases in this alloy following 500 hours at 1000˚C, Figure 4a, a high volume fraction of bright primary dendrites and a lower volume fraction of a dark interdendritic constituent. No further phases were observed at higher magnifications using SEM imaging,

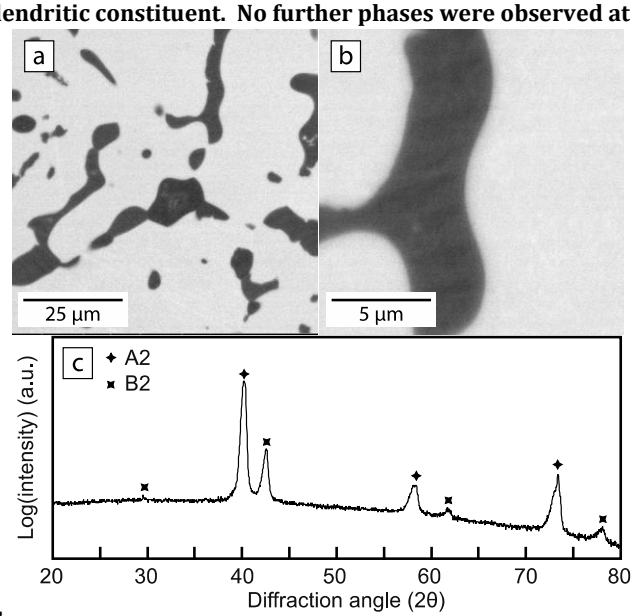

Figure **4**b.

The composition of the bright and dark phases were determined to be 60.3±0.4Ti-11.5±0.2Fe-28.3±0.4Mo and 51.4±0.2Ti-45.0±0.2Fe-3.6±0.1Mo respectively. These compositions were consistent with them being the A2 and B2 phases, from the previously reported phase diagrams shown in Figure 1.

The XRD spectrum obtained from alloy TF20M20, shown in

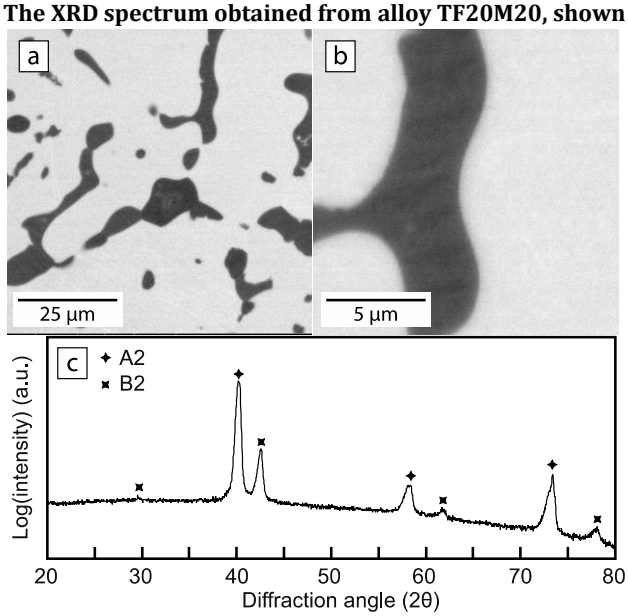

Figure **4**c, contained reflections corresponding to both A2 and B2 phases. Pawley refinement of the diffraction spectrum gave a lattice of a_{A2} = 3.17 ± 0.01 Å for the A2 phase, and a_{B2} = 3.00 ± 0.01 Å for the B2 phase, Table 3. As with alloy TF20M10, the areas under the B2 reflections were smaller than those of the A2 reflections, suggesting a lower volume fraction of the B2 phase. This was in line with the secondary darker phase observed in the BSE micrographs being B2 and in agreement with its composition determined by SEM-EDX. However, as

with alloy TF20M10, closer inspection of each of the A2 diffraction peaks identified reflections from a third phase at lower diffraction angles. Examination of alloy TF20M20 using TEM revealed selected area diffraction patterns and dark field micrographs akin to those seen for alloy TF20M10 in

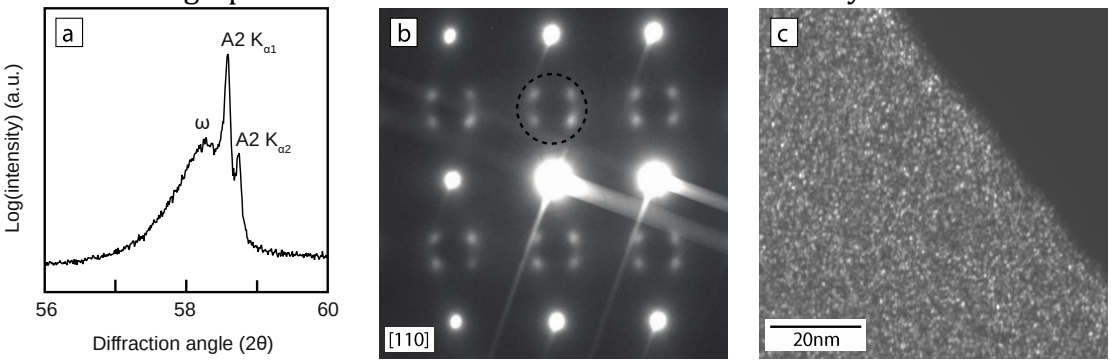

Figure **3**b and c.

3.3 TF20M40

Alloy TF20M40 was found to have a bulk composition of 37.6Ti-19.8Fe-42.6Mo. A BSE micrograph of alloy TF20M40 after 500 hours at 1000˚C is shown in

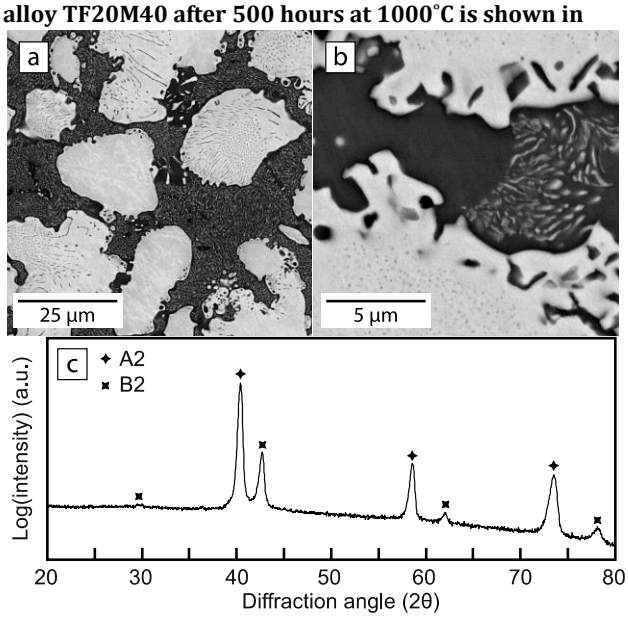

Figure 5**a, in which coarse, bright islands of primary dendrites could be observed, enveloped by a darker phase. Higher magnification imaging,**

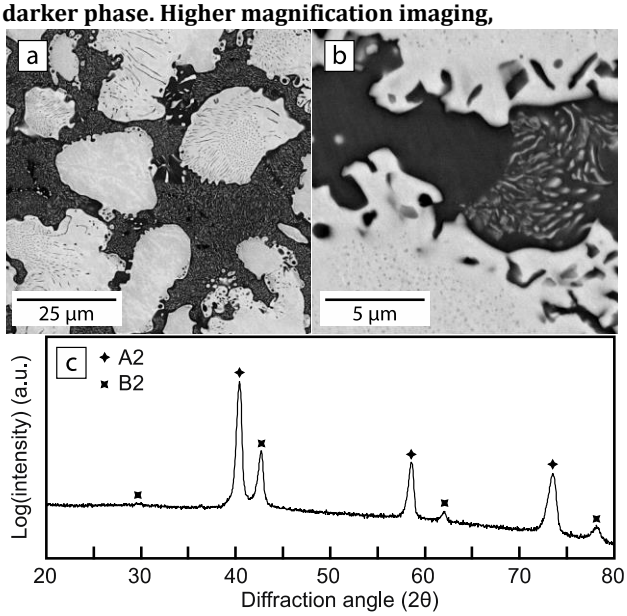

Figure **5**b, revealed the presence of fine dark and bright phases distributed within certain regions of both of the coarse phases. SEM-EDX analysis of the coarse bright phase in regions devoid of any fine phases, gave a composition of 32.1±1.2Ti-4.4±0.4Fe-63.5±1.1Mo, whilst analysis of the dark phase gave a composition of 49.9±0.3Ti-46.8±0.3Fe-3.3±0.1Mo. Through reference to

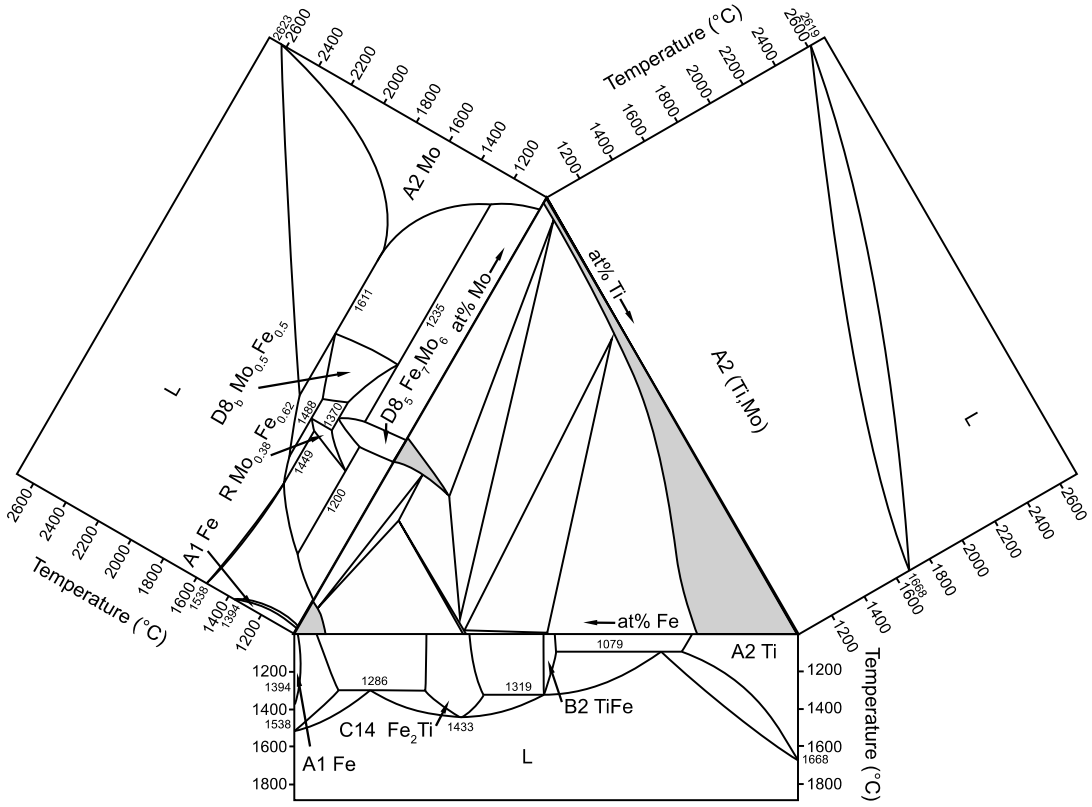

Figure **1**, these compositions were attributed to the A2 and B2 phases respectively.

The XRD spectrum obtained from alloy TF20M40, shown in

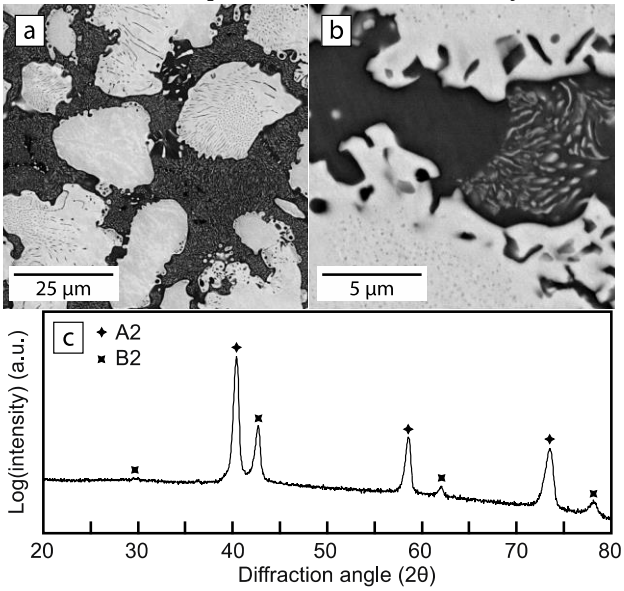

Figure 5**c, contained reflections from A2 and B2 phases only. Pawley refinement of the diffraction spectrum gave a lattice of a_{A2} = 3.15 ± 0.01 Å for the A2 phase, and a_{B2} = 2.99 ± 0.01 Å for the B2 phase, Table 3. In contrast to alloys TF20M10 and TF20M20, no diffraction peaks were observed consistent with the presence of incommensurate omega. As reflections were observed for only two phases it was concluded that all of the phases identified in the BSE micrographs,**

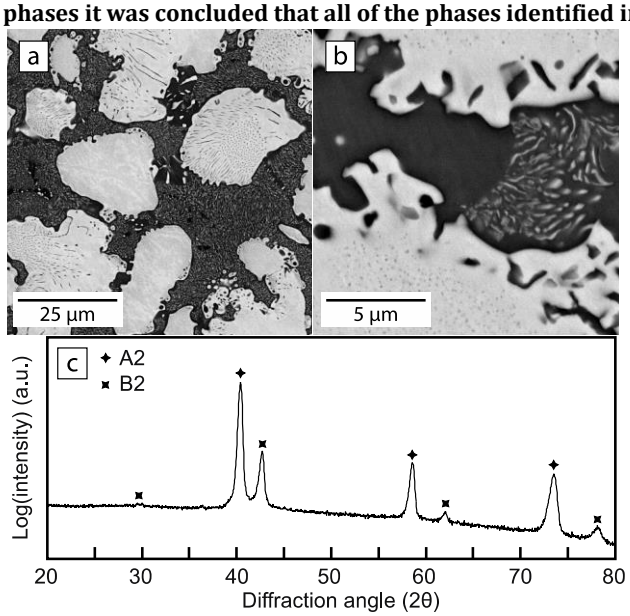

Figure **5**b, were either A2 or B2. The fine, bright phase was observed to have similar contrast to the coarse, bright phase, suggesting they were both A2, and, similarly, that both dark phases were B2.

SEM-EDX spectra taken in the regions containing fine phases inevitably resulted in sampling of both the fine phase and the surrounding matrix due to the size of the probe. The resulting compositions for these two-phase measurements were found to be intermediate between the compositions determined for the coarse A2 and B2 phases, which supports the conclusions drawn from the XRD data.

To determine the composition of the phases in isolation, STEM-EDX was used [34-36]. This was performed within domains containing coarse A2 and B2 phases to allow sampling of each phase in isolation. With this technique, the

composition of the A2 phase was determined to be 29.2±0.4Ti-3.2±0.2Fe-67.6±0.5Mo whilst that of the B2 phase was 47.9±0.5Ti-49.1±0.3Fe-3.0±0.3Mo. The A2 phase composition showed a markedly lower Fe concentration than that obtained using SEM-EDX, which suggested that the SEM-EDX probe may have partially sampled the B2 phase when attempting to analyse only the A2 phase. Similarly, the B2 composition was lower in Fe and Mo, indicating there may have been partial A2 sampling in the SEM-EDX measurement. The solubility of Mo in the B2 TiFe intermetallic compound has been debated by other authors, with some reporting it as a line compound with zero solubility and others suggesting it has solubility of up to 13 at.% [7,14,27]. The analysis performed in this study indicated that the limit of solubility for Mo in the B2 phase was 3 at.% at 1000°C.

3.4 TF20M60

Alloy TF20M60 was found to have a bulk composition of 17.8Ti-19.4Fe-62.8Mo. A BSE image showing the microstructure of this alloy following exposure at 1000°C for 500 hours is presented in

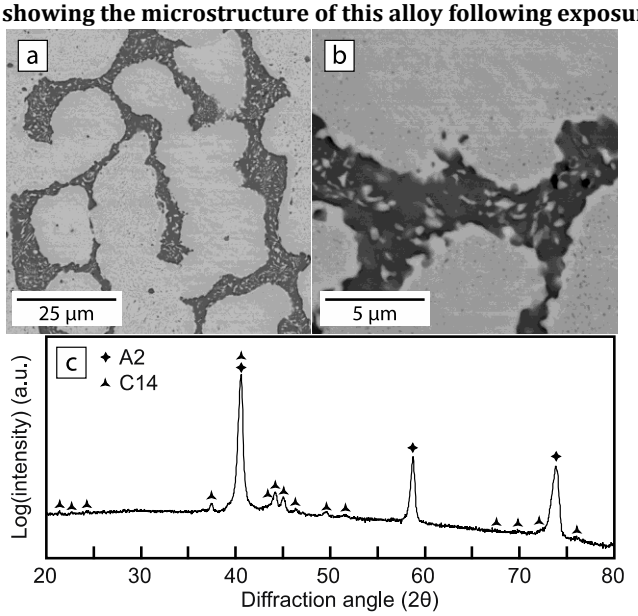

Figure 6**a. Bright primary dendrites were observed, surrounded by a darker phase, which was present in a lower volume fraction. Within this darker phase a fine bright phase was observed, as can be seen in the higher magnification image in**

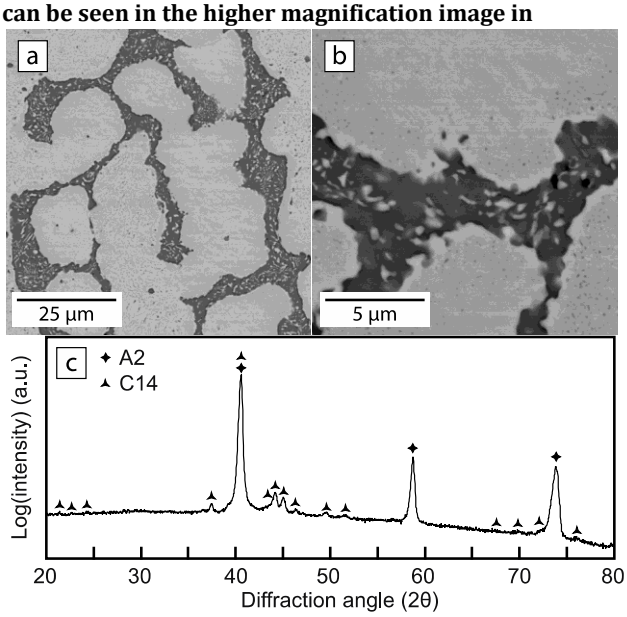

Figure **6**b.

The XRD spectrum collected from the alloy is shown in

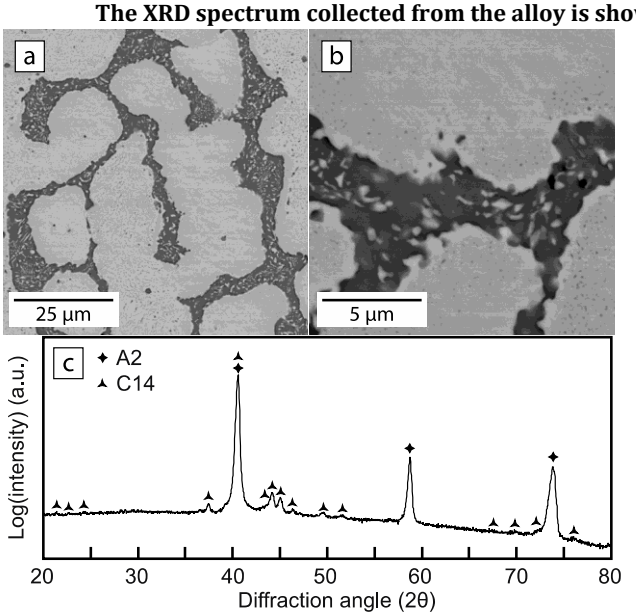

Figure **6**c. Reflections were observed consistent with the presence of an A2 phase, as well as reflections from a C14 phase. The lattice parameters of these phases obtained from Pawley fitting of the diffraction spectrum are given in Table 3. Comparison of the peak areas, suggested that the primary phase in the alloy was A2, with a lower volume fraction of the C14 phase. This result suggested that the primary high volume fraction bright phase was the A2 phase, whilst, in contrast to alloys TF20M10, TF20M20 & TF20M40, the darker phase was C14.

Given the appreciable volume fraction of the fine bright phase observed within the dark C14 phase,

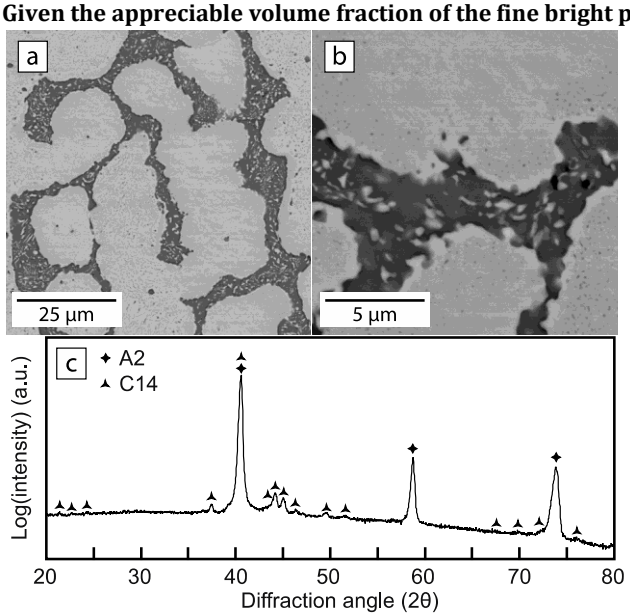

Figure **6**b, a contribution to the XRD spectrum would be expected. However, as only reflections from A2 and C14 phases could be identified, combined with the observation that the fine phase had similar contrast to the primary coarse A2 phase, it was considered likely that the fine bright phase was also A2.

Compositional analysis, performed using SEM-EDX, produced values of 14.1±2.2Ti-3.4±0.3Fe-81.6±2.3Mo for the bright A2 phase and 29.2±0.7Ti-

63.8±1.6Fe-7.0±1.4Mo for the darker C14 phase. However, as with alloy TF20M40, the small size of the bright phase within the C14 matrix prohibited unambiguous compositional measurement using SEM-EDX. Despite this limitation, the compositions obtained were intermediate between those of the C14 and A2 phases, suggesting that the fine bright phases were indeed A2.

STEM-EDX analysis gave compositions of 12.6±0.7Ti-1.9±0.3Fe-85.5±0.9Mo for the A2 phase and 26.3±1.2Ti-65.2±2.8Fe-8.5±3.8Mo for the C14 phase. The A2 composition obtained using STEM-EDX was leaner in Fe than that measured using SEM-EDX, whilst the C14 composition determined by STEM-EDX was richer in Fe. These observations suggest that the compositions of both the A2 and C14 phases obtained by SEM-EDX may have suffered from partial sampling of the other phase.

Extensive sampling of alloy TF20M60 identified a region within which a three-phase microstructure existed, as shown in Figure 7a and b. The local composition of this region was measured by a large area SEM-EDX scan and found to be 16.6Ti-19.6Fe-63.8Mo, which was slightly richer in Mo and leaner in Ti than the average composition of this alloy, given in Table 2. The compositions of the three phases in this local region were evaluated by SEM-EDX and determined to be 12.1±0.2Ti-2.8±0.3Fe-85.1±0.5Mo for the bright phase, 27.1±0.3Ti-64.4±0.4Fe-8.4±0.2%Mo for the dark phase and 22±0.6Ti-53.8±0.7Fe-24.2±1.1Mo for the grey phase. Comparison of these results with the ternary phase diagram shown in Figure 1 suggested that these phases were A2, C14 and $D8_5$ respectively.

3.5 TF20M70

Alloy TF20M70, with a bulk composition of 9.7Ti-19.3Fe-70.9Mo, was the most Mo rich of the alloys studied. In the BSE micrograph of the alloy, shown in

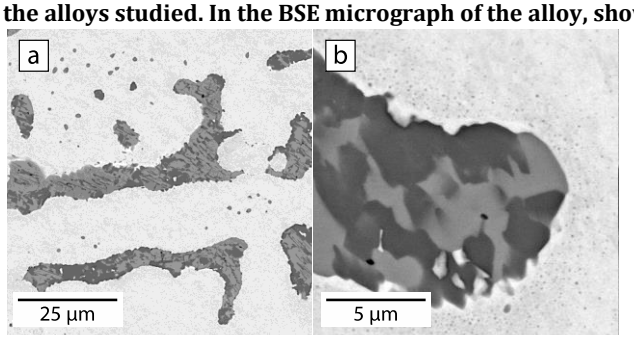

Figure 7 – Alloy TF20M60: BSE micrographs of a region containing the A2, C14 and $D8_5$ phases, a) overview and b) detailed view.

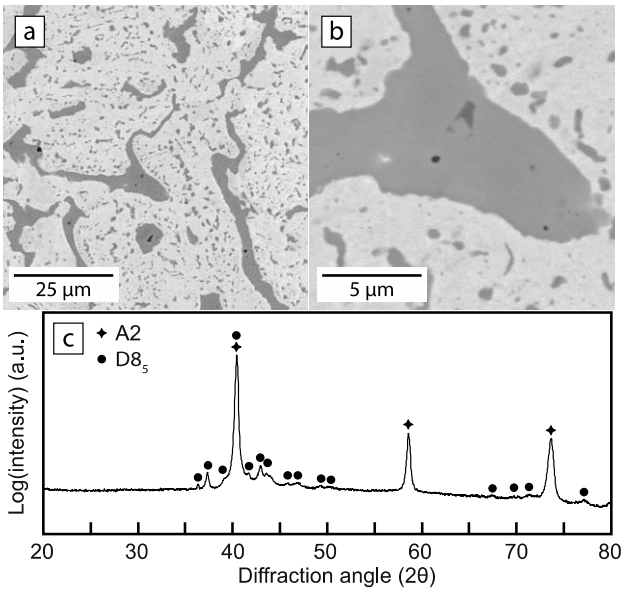

Figure 8**a, a bright majority phase, corresponding to the prior dendrites, was found to be in equilibrium with a lower volume fraction of a grey phase, which was distributed both between and finely within the bright phase. In addition, within the grey phase, fine isolated pockets of a darker phase were observed, as shown in the magnified image presented in**

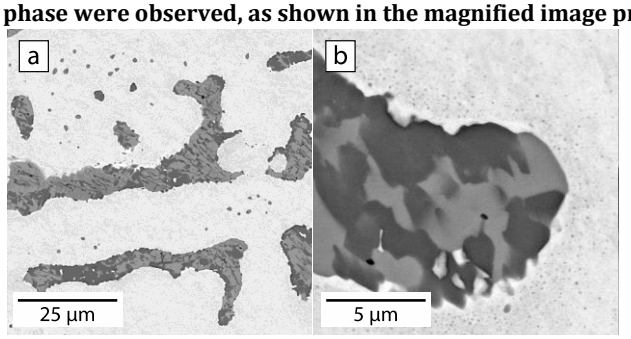

Figure 7 – Alloy TF20M60: BSE micrographs of a region containing the A2, C14 and $D8_5$ phases, a) overview and b) detailed view.

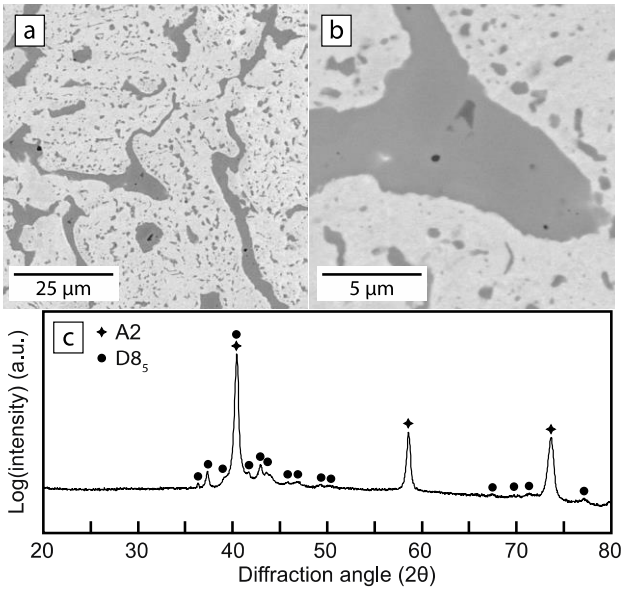

Figure **8**b.

The XRD spectrum for the alloy is shown in

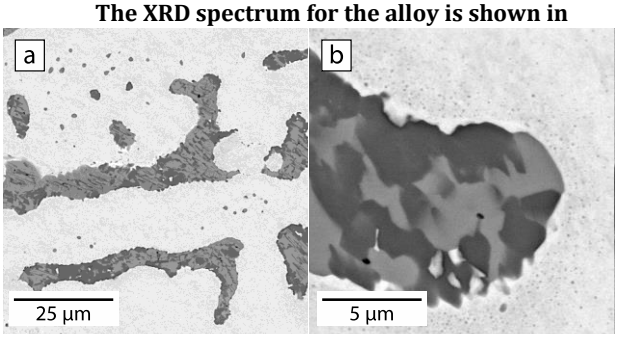

Figure 7 – Alloy TF20M60: BSE micrographs of a region containing the A2, C14 and $D8_5$ phases, a) overview and b) detailed view.

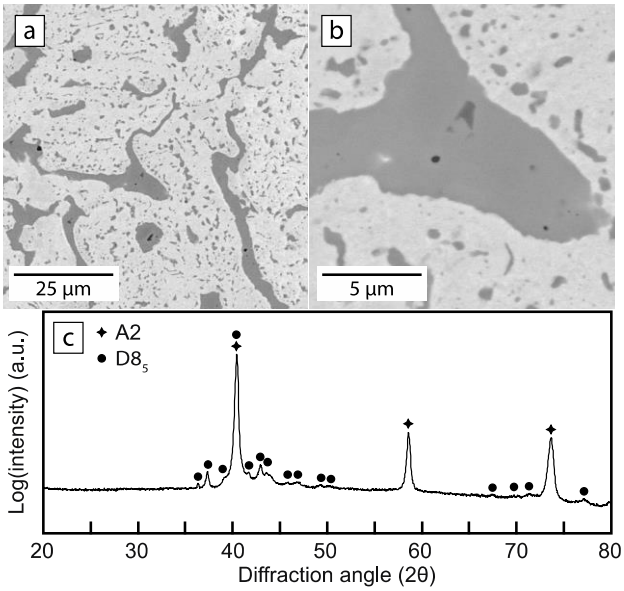

Figure 8**c. The strongest reflections were consistent with the presence of an A2 phase. Lower intensity peaks were also observed from a $D8_5$ phase. Whilst the $D8_5$ and C14 phases have many reflections at similar angles, the lack of the characteristic peaks between 20 and 25° 2θ, seen in**

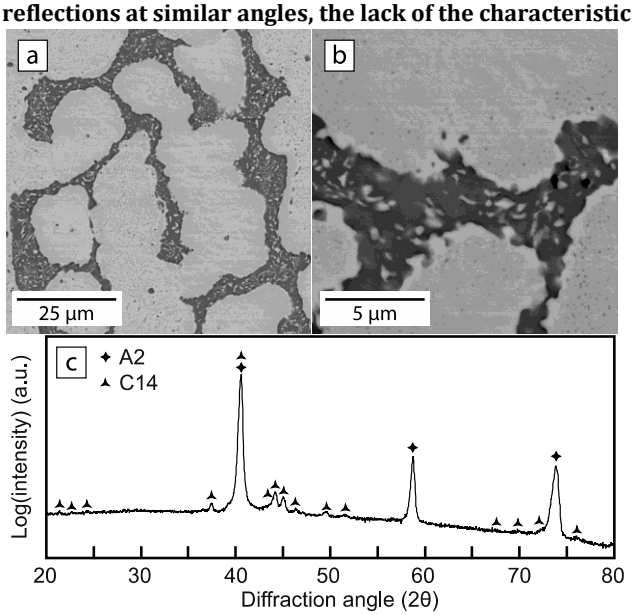

Figure **6**c, indicated that, if present, the C14 phase must constitute a much lower volume fraction that either the A2 or $D8_5$ phases. The lattice parameters of the

phases obtained from Pawley fitting of the diffraction spectrum are given in Table 3.

SEM-EDX analysis of the bright phase gave a composition of 7.8±0.4Ti-2.5±0.7Fe-89.7±0.9Mo, whilst sampling of the grey phase gave a composition of 14.6±0.8Ti-52.9±0.4Fe-32.4±1.0Mo. These compositions are consistent with the A2 and $D8_5$ phases respectively. The small darker phase, seen in

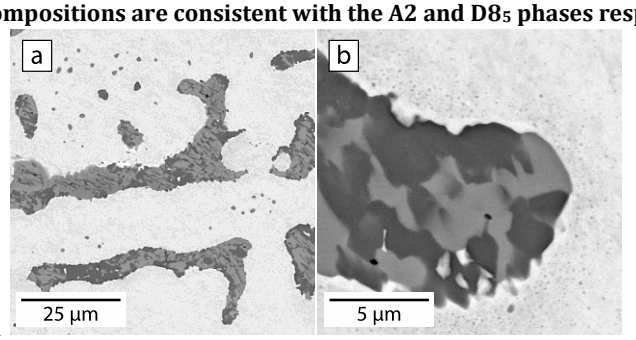

Figure 7 – Alloy TF20M60: BSE micrographs of a region containing the A2, C14 and $D8_5$ phases, a) overview and b) detailed view.

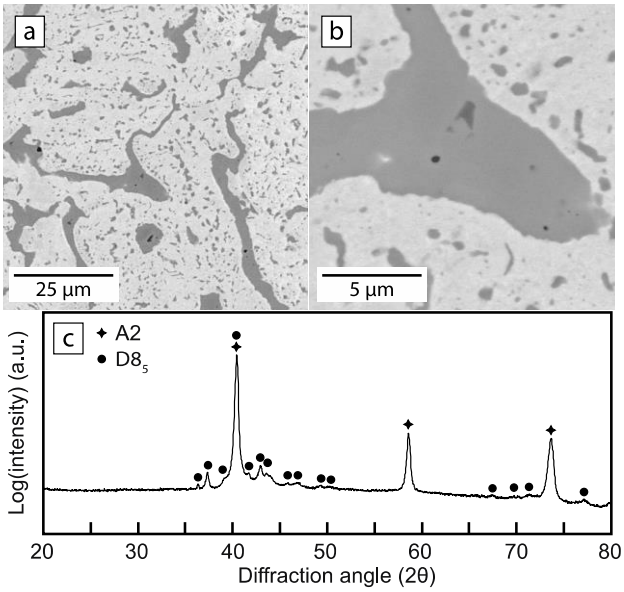

Figure **8**b, could not be sampled in isolation by SEM-EDX. However, the results indicated that this phase was lower in Mo than the $D8_5$ phase and approached the composition of the C14 phase measured in alloy TF20M60. Therefore, it is likely that the darker phase was the C14 phase, and that this was in local equilibrium with the $D8_5$ phase that enveloped it. Crucially, the dark C14 phase was never observed in contact with the A2 phase and so does not support the possibility that the three phases exist in equilibrium within this alloy.

STEM-EDX analysis of the phases present was performed, from which the composition of the A2 phase was determined to be 7.3±0.1Ti-2.0±0.1Fe-90.7±0.3Mo and the composition of the $D8_5$ phase was found to be 12.3±0.4Ti-58.1±1.5Fe-29.6±1.4Mo. Unfortunately, no regions containing the C14 phase were found in any of the TEM foils prepared from this alloy.

3.6 TF60M10

The bulk composition of alloy TF60M10 was determined to be 29.7Ti-59.8Fe-10.5Mo. The microstructure, shown in

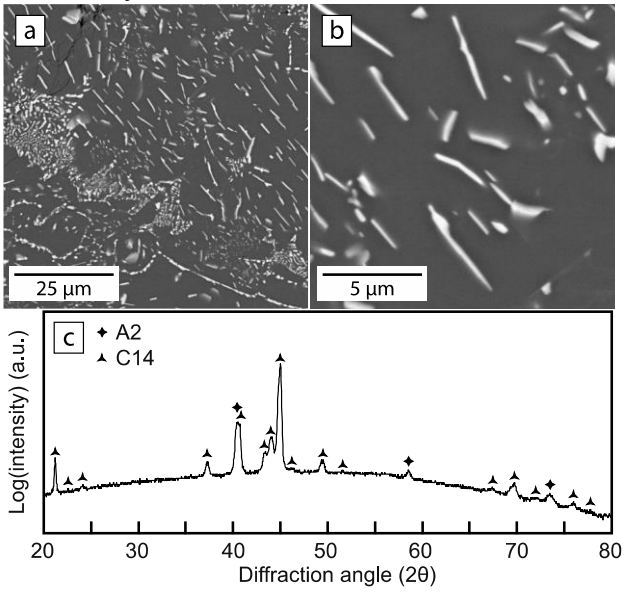

Figure 9**a, was dramatically different to those of the alloys described previously. A dark matrix phase was observed, within which were fine bright laths of a second phase with a low volume fraction. These can be seen more clearly in the higher magnification image presented in**

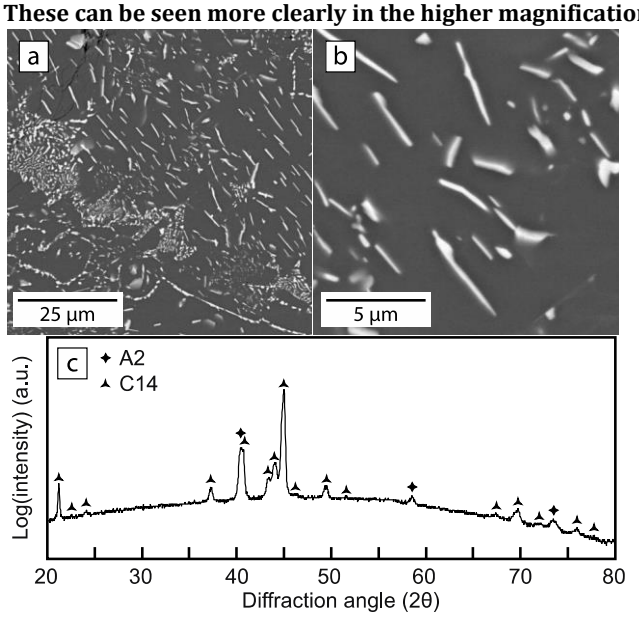

Figure **9**b. In some regions, these fine laths were widely separated, whilst in others they were clustered, with the clustered regions seeming to correspond to the prior interdendritic areas.

The XRD spectrum obtained from the alloy is shown in Figure 9c, in which reflections from C14 and A2 phases were identified. Comparison of the peak areas of the two phases suggested that the C14 phase had a larger volume fraction and, therefore, that it was the dark matrix phase, whilst the fine, bright laths were the A2 phase. The lattice parameters of the phases obtained from Pawley fitting of the diffraction spectrum are given in Table 3.

The composition of the C14 matrix was found by SEM-EDX to be 31.4±0.2Ti-63.4±0.3Fe-5.2±0.4Mo. Attempts to sample the fine bright A2 laths using SEM-EDX gave a composition of 24.1±1.6Ti-31.9±6.8Fe-44.1±8.4Mo. However, there was large scatter in this measurement as indicated by the

associated uncertainty, due to incompatibility between the probe and features sizes. STEM-EDX analysis gave a composition of 15.2±0.9Ti-3.9±0.6Fe-81.0±1.4Mo for the A2 laths, and 29.3±0.7Ti-66.3±0.4Fe-4.4±1.0Mo for the C14 matrix. These two compositions were close to those of the A2 and C14 phases measured in alloy TF20M60, indicating that the two alloys lay on a similar tie line and provided further confirmation that the laths were A2.

3.7 TF33M33

Alloy TF33M33 was found to have a bulk composition of 36.7Ti-31.7Fe-31.6Mo. In the BSE micrograph obtained from this alloy following 500 hours at 1000˚C, shown in

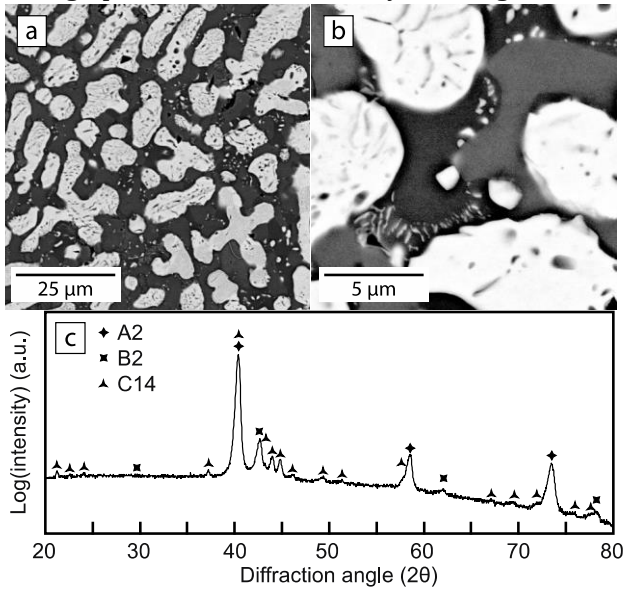

Figure 10**a, bright primary dendritic regions were observed surrounded by an extensive dark interdendritic constituent. Fine dark particles were also identified within the primary bright phase and vice versa. These can be seen more clearly in the higher magnification image shown in**

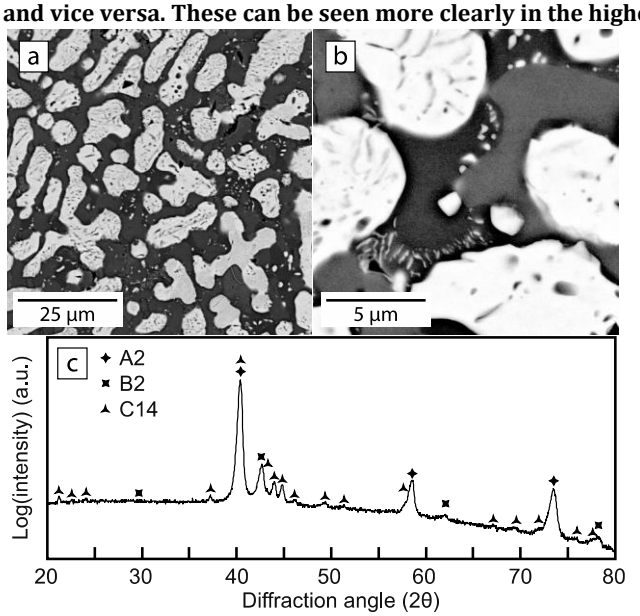

Figure **10**b. Careful contrast adjustment, leading to oversaturation of the bright phase, revealed that the coarse dark region actually contained an intermediate grey phase as well as a dark phase. This indicated that the alloy contained three phases in equilibrium, with the bright phase present with a higher volume

fraction than the dark and grey phases, which were present in roughly equal proportions.

The corresponding XRD spectrum, shown in

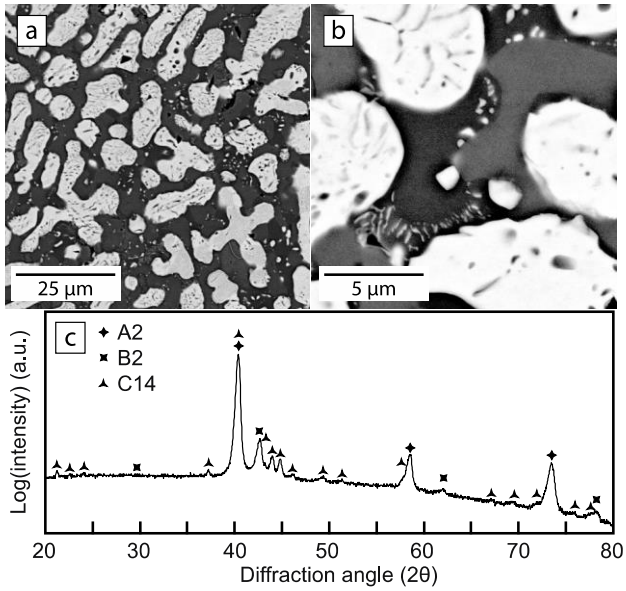

Figure 10**c, supports the observation of three phases, with diffraction peaks from A2, B2 and C14 phases being identified. The A2 peaks have the greatest area suggesting that this was the primary bright phase observed by SEM. The lattice parameters of the phases obtained from Pawley fitting of the diffraction spectrum are given in Table 3. Compositional analysis of the three phases was performed by taking EDX spectra at triple junctions. With this approach, the composition of the bright A2 phase was determined to be 22.1±0.7Ti-2.9±0.4Fe-75.0±1.0Mo, whilst that of the dark phase was 49.4±0.9Ti-46.8±0.9Fe-3.8±0.5Mo, and the grey phase was 35.2±0.4Ti-61.3±0.5Fe-3.5±0.5Mo. Comparing these compositions to those of phases in the Ti-Fe binary system (Table 1,**

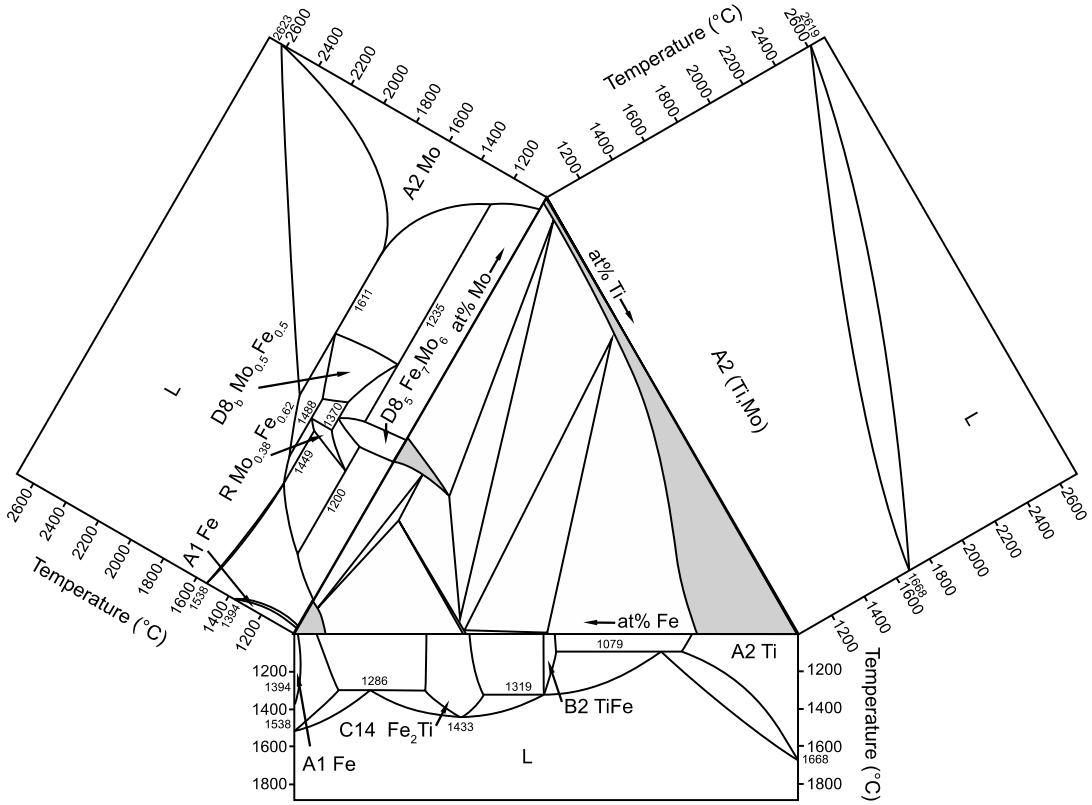

Figure 1**) indicated that the dark phase was B2 TiFe, and the grey phase was C14 Fe_2Ti, with each**

intermetallic phase containing a small amount of Mo. The fine bright features within the dark phase,

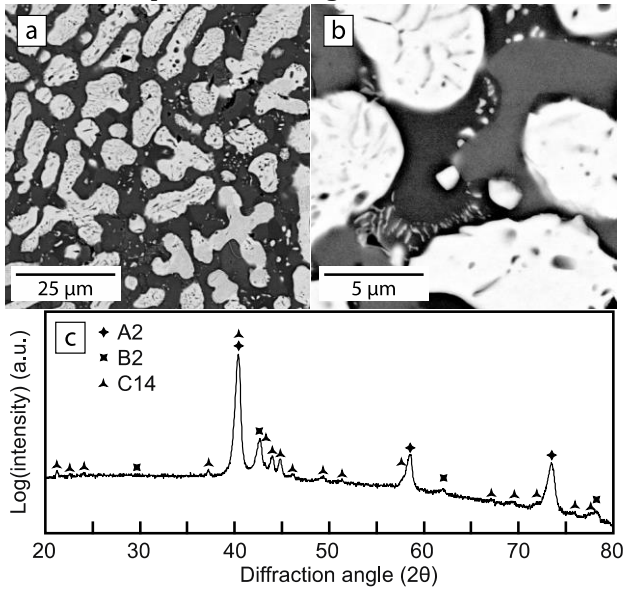

Figure **10**b, had a similar contrast to the A2 dendrites and so were considered likely to be the same phase. However, the dark features seen within the A2 dendrites could not be unambiguously identified as being either the B2 or C14 phases, as their imaging contrast was insufficiently distinct.

STEM-EDX analysis was performed, from which the compositions of the constituent phases were: 22.1±1.3Ti-3.5±0.2Fe-74.5±1.4Mo for the bright A2 phase, 48.9±0.4Ti-48.8±0.2Fe-2.3±0.4Mo for the dark B2 phase, and 34.3±0.3Ti-63.4±0.5Fe-2.3±0.6Mo for the grey C14 phase. These compositions were in good agreement with the SEM-EDX results.

4.0 Discussion

The stable phases found in each of the alloys and their compositions are summarised in Table 3. Alloys TF20M10, TF20M20 and TF20M40 were all found to be two-phase A2+B2, whilst alloy TF20M60 was A2+C14, alloy TF60M10 was C14+A2 and alloy TF20M70 was A2+$D8_5$. Alloy TF33M33 lay in the A2+B2+C14 three-phase field. This implied an A2+C14+$D8_5$ three-phase field also existed and a localised region of alloy TF20M60 was found to contain these three phases in equilibrium.

The 1000°C isothermal section of the Fe-Mo-Ti ternary phase diagram determined from these experimental results is shown in Figure 11. Tie lines and tie triangles were included linking the compositions of phases that were found to be in equilibrium with each other. The measured compositions for each of the melted alloys, given in Table 2, were also plotted. The composition of each of the binary phases at 1000˚C, taken from the assessments of Houserova *et al*. [25], Dumitrescu *et al*. [21] and Franke & Neuschütz [6], were included. These results were used in combination with the experimental data to determine the locations of each of the phase boundaries by interpolating between them. This resulted in continuous boundaries for the A2 and B2 phases, as well as partial boundaries for the $D8_5$ and C14 phases. For the coarse phases, the SEM-EDX and STEM-EDX data were weighted similarly, whilst considering the variance identified in Table 3. For the fine A2 and B2 phases in TF20M40 and the laths of the A2 phase in TF60M10, SEM-EDX was unable to sample these phases in isolation and so a

higher weighting was applied to the STEM-EDX data. Where no data was available from the current assessment, tentative dotted boundaries have been included. These are based on information from the most recent binary assessments and the previous ternary assessments [6-16].

The 1000°C isothermal section of the Fe-Mo-Ti ternary system in Figure **11** shows several key features. First, the solubility of Fe in the continuous A2 (Ti, Mo) phase reduced as the Mo content increased, consistent with previous reports [14]. Second, the extension of the B2 phase field into ternary composition space was limited to ~ 3 at.% Mo, which is significantly lower than that reported by Sokolovskaya *et. al.* [7]. Third, the $D8_5$ phase shows a greater solubility for Ti, ~22 at.%, than reported previously. The composition of the $D8_5$ phase in alloy TF20M60 was $Fe_{6.99}Mo_{3.15}Ti_{2.86}$, which indicates that the phase closely follows the formula $Fe_7(Mo, Ti)_6$. Fourth, the range of compositions measured for the C14 phase suggests that Mo is exchanged for Ti following the formula $Fe_2(Mo, Ti)$. These results, in addition to the more recent Ti-Fe binary assessments [15,21] that indicate 1-2 at.% (Ti, Mo) can be tolerated on the Fe sites, demonstrate that the $Fe_2(Ti, Mo)$ phase should not considered as a line compound. Fifth, the A2+C14 two-phase field is far thinner than previous assessments, whilst the A2+$D8_5$ and A2+B2 two-phase fields are more extensive. As a direct consequence, the A2+ $D8_5$+C14 three-phase, in the current study, was found to be exceedingly narrow.

5.0 Conclusions

The phase equilibria in the Fe-Mo-Ti ternary system have been evaluated through the study of seven bulk alloys. These were heat treated at 1000°C for 500 hours and experimentally evaluated in order to determine an isothermal section of the Fe-Mo-Ti ternary phase diagram.

Phases were identified and analysed by SEM, SEM-EDX, TEM, STEM-EDX and XRD. Of the reflections seen in the XRD spectra for each alloy, all of the peaks observed were accounted for, confirming that no A1 Fe, A2 Fe, A3 Ti structured phases, nor any ternary phases existed in the alloys analysed. Additional peaks seen in the XRD spectra of the Ti rich alloys prompted further study by TEM, which identified nanoscale domains attributed to incommensurate omega that formed on cooling.

The positions of the A2+B2+C14 and A2+C14+$D8_5$ phase fields were determined from the compositions of the three constituent phases measured at triple junctions. These data also served to identify the extents of the A2+B2, A2+$D8_5$, A2+C14, C14+B2 and C14+$D8_5$ two-phase fields, as well as the ternary solubility limits of the A2, B2 and $D8_5$ phases. The $D8_5$ phase extends into ternary space following the formula $Fe_7(Mo, Ti)_6$, whilst the C14 phase was seen to follow the formula $Fe_2(Ti, Mo)$ across the composition range studied. The $D8_5$, C14 and B2 intermetallic phases were found to tolerate up to 3 at.%, off-stoichiometric compositions and, as such, should not be considered line compounds.

Acknowledgements
The authors wish to extend their thanks to: K. Roberts, for encapsulation of the samples, as well as M. Vickers and A. Moss, for assistance with XRD. This work was support by the Rolls-Royce/EPSRC Strategic Partnership under EP/H022309/1, EP/H500375/1 and EP/M005607/1.

References

1. Louzguine, D. V., Kato, H. & Inoue, A. High strength and ductile binary Ti–Fe composite alloy. Journal of Alloys and Compounds, 384, L1–L3 (2004).
2. Das, J. et al. Bulk ultra-fine eutectic structure in Ti–Fe–base alloys. Journal of Alloys and Compounds, 434-435, 28–31 (2007).
3. Louzguine-Luzgin, D. V., Louzguina-Luzgina, L. V., Kato, H. & Inoue, A. Investigation of high strength metastable hypereutectic ternary Ti–Fe–Co and quaternary Ti–Fe–Co–(V, Sn) alloys. Journal of Alloys and Compounds, 434-435, 32–35 (2007).
4. Das, J., Theissmann, R., Löser, W. & Eckert, J. Effect of Sn on microstructure and mechanical properties of Ti-Fe-(Sn) ultrafine eutectic composites. Journal of Materials Research, 25, 943–956 (2010).
5. Cao, G. H. et al. Formation of a bimodal structure in ultrafine Ti–Fe–Nb alloys with high-strength and enhanced ductility. Proceedings of the Second International ASM Conference on High Temperature Aluminides and Intermetalics: Part 2, 609, 60–64 (2014).
6. Franke, P. & Neuschütz, D. Binary Systems. Part 4: Binary Systems from Mn-Mo to Y-Zr - Mo-Ti., 19B4, 1–4 (Springer Berlin Heidelberg, 2006).
7. Sokolovskaya, E. M., Kazakova, E. F., Gryzunov, B. I., Duisebaev, M. & Konysova, B. K. Interactions and properties of intermetallic phases in the Fe-Ti-Mo system at 900°C. Vestnik Moskovskogo Universiteta Serila II. Khimila 43, 404–405 (1988).
8. Watson, A. & Markus, T. Thermodynamic Properties of Inorganic Materials Compiled by SGTE, Subvolume C, Part 2. Chapter: Ternary System Fe-Mo-Ti. 152-161 (2015).
9. Raghavan, V. Fe-Mo-Ti (Iron-Molybdenum-Titanium), Journal of Phase Equilibria, 24, 2, 182-183 (2003).
10. English, J. J. Binary and ternary phase diagrams of columbium, molybdenum, tantalum, and tungsten. Defense Metals Information Center, AD 257 739, OTS P6 171421, DMIC Report 152 (1961).
11. Shurin, A. K., Dmitrieva, G. P. & Cherepova T. S. Phase Equilibria in Titanium-Rich Alloys of the Fe-Mo-Ti System. Powder Metallurgy and Metal Ceramics, 42, 9-10, 513-516 (2003).
12. Yamane T., Tani K., Wang Y.P., Inaba T. Omega phase precipitation in Ti-Fe, Ti-Mo, and Ti-Fe-Mo alloys. Journal of High Temperature Society of Japan, 10, 5, 194-199 (1984).
13. Raghavan, V. Phase diagrams of ternary iron alloys, part 6. 994–996 (Indian Institute of Metals, 1992).
14. Jin, Z. P. & Qiu, C. An Experimental-Study and Thermodynamic Evaluation of the Fe-Mo-Ti System at 1000 Degrees-C. Metallurgical Transactions A, 24, 2137–2144 (1993).

15. Hong, B. et al. Thermodynamic re-assessment of Fe–Ti binary system. Transactions of Nonferrous Metals Society of China, 22, 2204–2211 (2012).
16. Rajkumar, V. B. & Kumar, K. C. H. Thermodynamic modeling of the Fe-Mo system coupled with experiments and ab initio calculations. Journal of Alloys and Compounds, 611, 303–312 (2014).
17. Rudy, E. Comp. Phase Diagram Data, Ternary Phase Equil. TM-B-C-Si, AFML-Tr-65-2, Part V. (Aerojet-General Corporaton, 1969).
18. Saunders, N. COST 507, 'Thermochemical database for light metal alloys'. Office for Official Publications of the European Communities, 2, 249–252 (1998).
19. Kumar, K. C., Wollaiits, P. & Delaey, L. Thermodynamic reassessment and calculation of Fe-Ti phase diagram. CALPHAD, 18, 223–234 (1994).
20. Kovnyeristyy, K. Y., Boriskina, G. N., and Kyenina, M. Y. Metastable equilibria of the titanium alloys with iron, cobalt and nickel obtained by quenching from liquid state. Stabil'nye i Metastabil'nye Fazocye Ravnovesiya v Metallicheskikh Sistemakh, Nauka, Moscow, USSR, 158–160 (1985).
21. Dumitrescu, L. F. S., Hillert, M. & Sounders, N. Comparison of Fe-Ti Assessments. Journal of phase equilibria, 19, 441–448 (1998).
22. Murray, J. L. The Fe– Ti (Iron-Titanium) system. Bulletin of Alloy Phase Diagrams, 2, 320–334 (1981).
23. VanThyne, R. J., Kessler, H. D. & Hansen, M. The Systems Titanium-Chromium and Titanium-Iron. Transactions of the American Society of Metals, 44, 974–989 (1952).
24. Murakami, Y., Kimura, H. & Nishimura, Y. An Investigation of the Titanium-Iron-Carbon System. J. Japan Inst. Metals, 21, 669–673 (1957).
25. Houserová, J., Vřešťál, J. & Šob, M. Phase diagram calculations in the Co–Mo and Fe–Mo systems using first-principles results for the sigma phase. Calphad, 29, 133-139 (2005).
26. Guillermet, A. F. The Fe-Mo (Iron-Molybdenum) system. Bulletin of Alloy Phase Diagrams, 3, 3, 359-366 (1982).
27. Kamegawa, A., Kudo, H., Takamura, H. & Okada, M. Protium absorption and desorption properties of bcc Ti-Fe solid solution alloys stabilized by Mo addition. Materials Transactions, 44, 991–994 (2003).
28. Kanaya, K. & Okayama, S. Penetration and energy-loss theory of electrons in solid targets. Journal of Physics D: Applied Physics, 5, 43-58 (1972).
29. Nosova, G. I., D'yakonova, N. B. & Lyasotskii, I. V. Metastable phases of electron type in titanium alloys with 3d-metals. Metal Science and Heat Treatment, 48, 427-432 (2006).
30. Jones, N.G., Dashwood, R.J., Jackson, M., Dye, D., β Phase decomposition in Ti-5Al-5Mo-5V-3Cr, Acta Materialia, 57, 13, 3830-3839 (2009).
31. Bennett, J.M., Barnard, J.S., Stone, H.J., Midgley, P.A., Rugg, D., Jones, N.G., On the nature of the omega tri-layer periodicity in rapidly cooled Ti-15Mo, Scripta Materialia, 107, 79-82 (2015).
32. De Fontaine, D. Mechanical instabilities in the bcc lattice and the beta to omega phase transformation. Acta Metallurgica, 18, 275-279 (1970).
33. Sikka, S. K., Vohra, Y. K. & Chidambaram, R. Omega phase in materials. Progress in Materials Science, 27, 245-310 (1982).

34. Matera, S. & Anelli, E. TEM-EDS characterization of second phases in ferritic steels. Microscopy Microanalysis, 6, 633-646 (1995).
35. Williams, D. B. & Carter, C. B. Transmission Electron Microscopy. (Springer US, 2009).
36. Cliff, G. & Lorimer, G. W. The quantitative analysis of thin specimens. Journal of Microscopy, 103, 203-207 (1975).

Figures

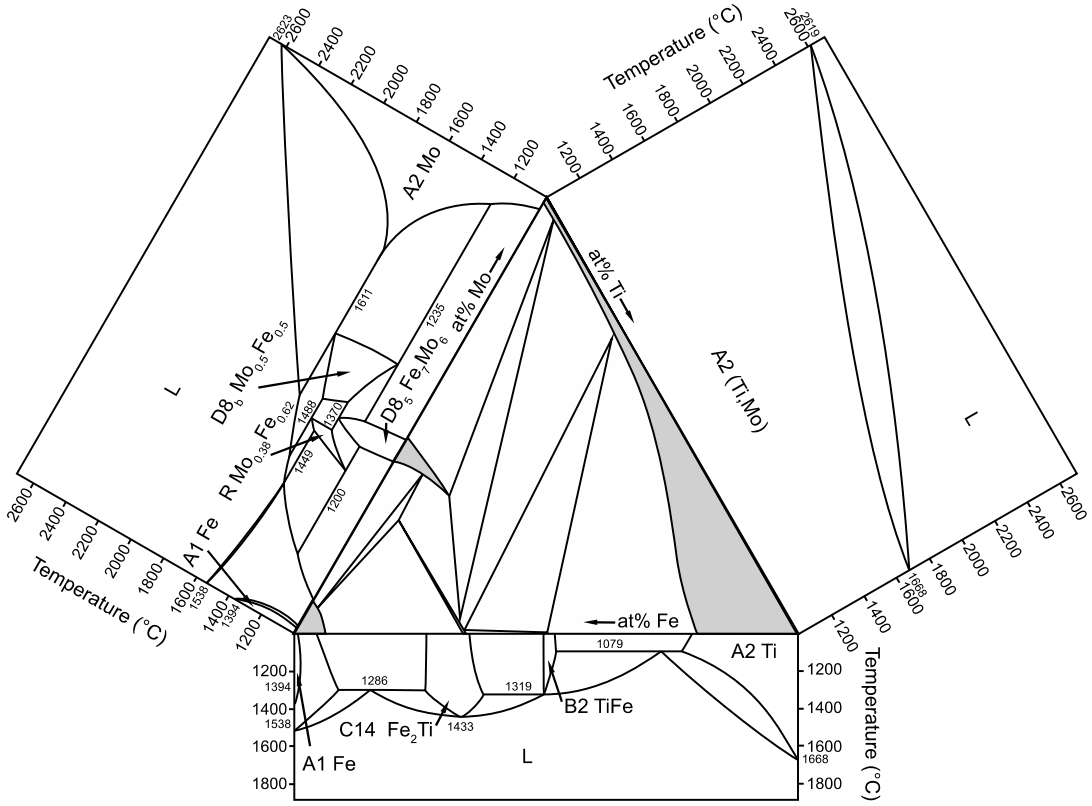

Figure 1 – Compilation of the Fe-Ti [15], Fe-Mo [16] and Mo-Ti [6] binary phase diagrams and the Fe-Mo-Ti [8] ternary phase diagram.

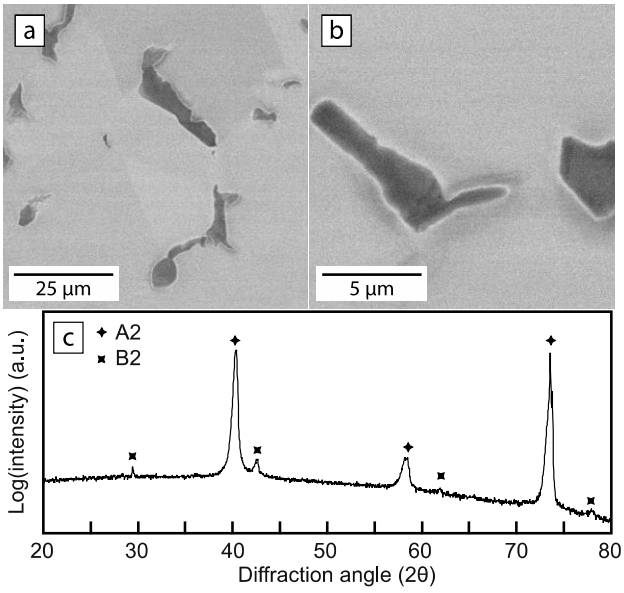

Figure 2 – Alloy TF20M10: BSE micrographs, a) overview and b) detailed view, as well as c) a XRD spectrum.

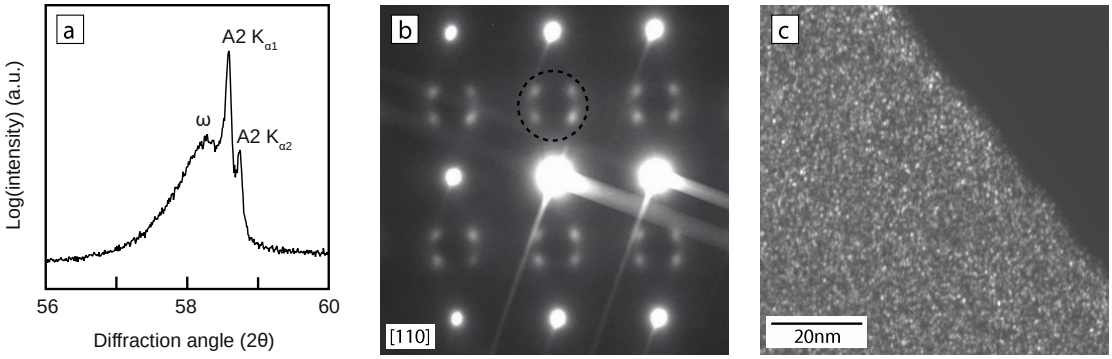

Figure 3 - Alloy TF20M10: a) detailed XRD spectrum, b) SADP taken within A2 phase, c) DF taken using the spots identified in b)

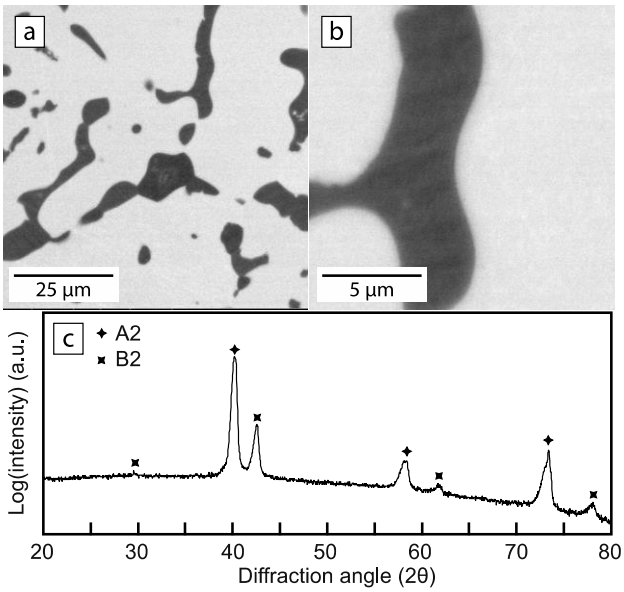

Figure 4 - Alloy TF20M20: BSE micrographs, a) overview and b) detailed view, as well as c) a XRD spectrum.

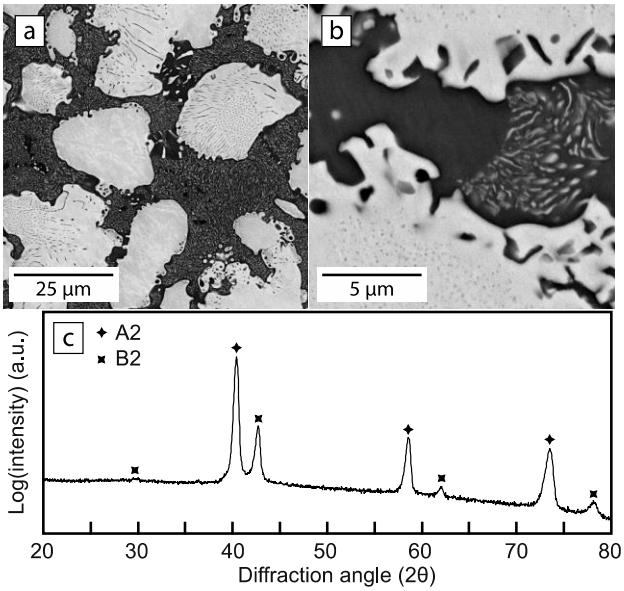

Figure 5 - Alloy TF20M40: BSE micrographs, a) overview and b) detailed view, as well as c) a XRD spectrum.

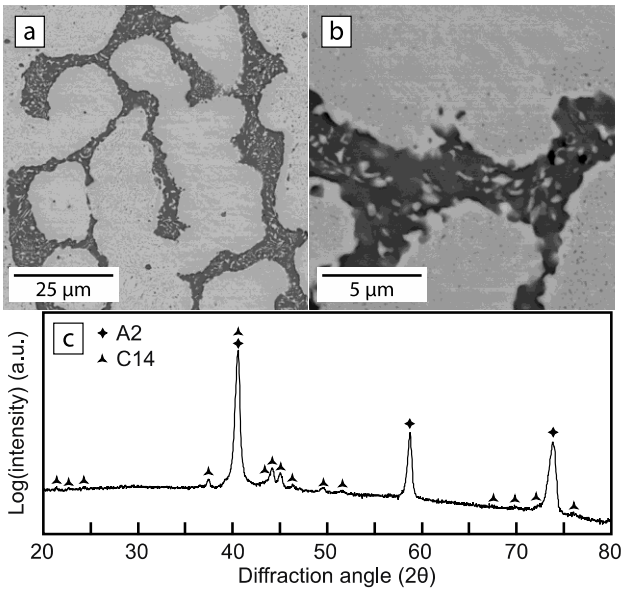

Figure 6 – Alloy TF20M60: BSE micrographs, a) overview and b) detailed view, as well as c) a XRD spectrum.

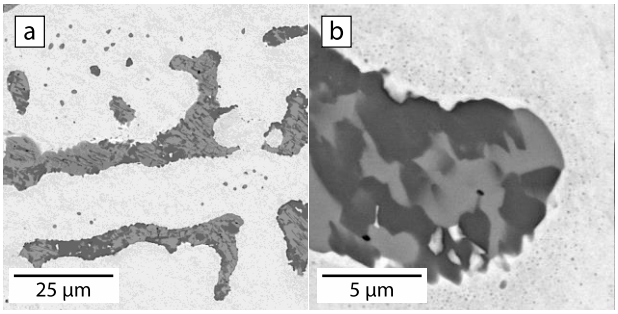

Figure 7 – Alloy TF20M60: BSE micrographs of a region containing the A2, C14 and $D8_5$ phases, a) overview and b) detailed view.

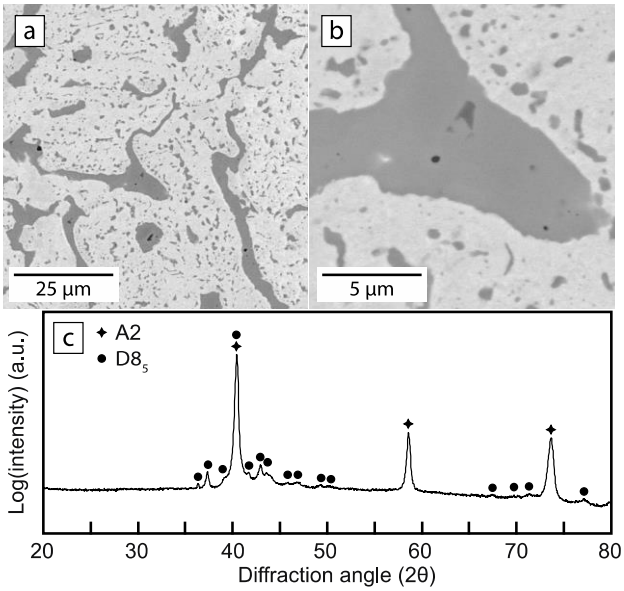

Figure 8 – Alloy TF20M70: BSE micrographs, a) overview and b) detailed view, as well as c) a XRD spectrum.

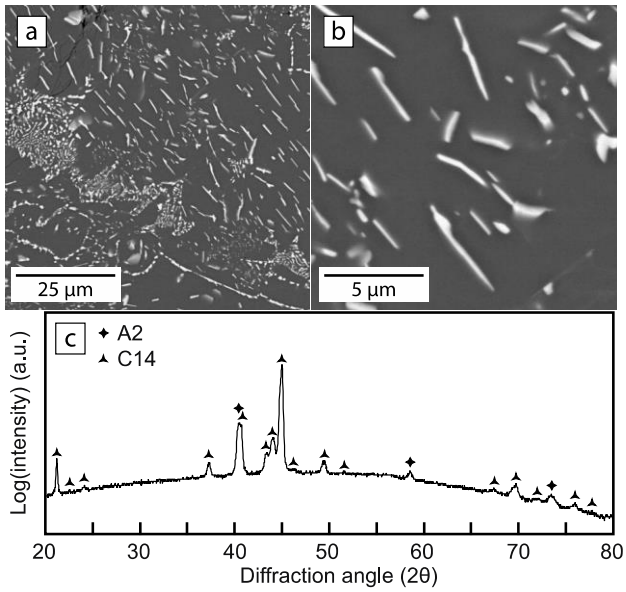

Figure 9 – Alloy TF60M10: BSE micrographs, a) overview and b) detailed view, as well as c) a XRD spectrum.

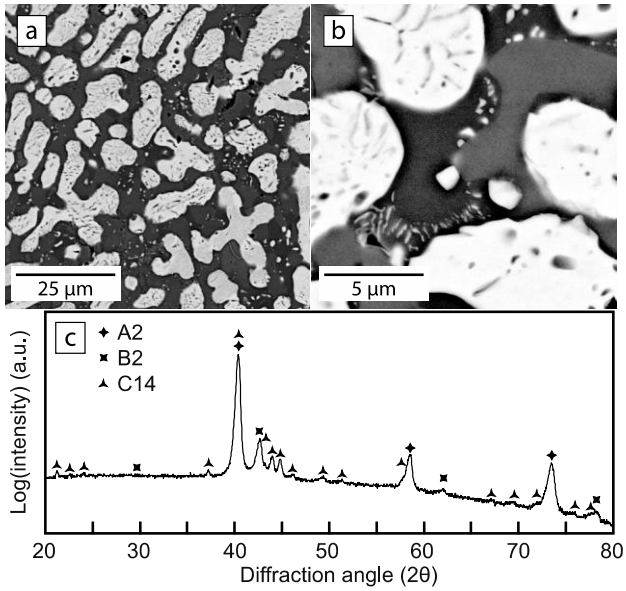

Figure 10 – Alloy TF33M33: BSE micrographs, a) overview and b) detailed view, as well as c) a XRD spectrum.

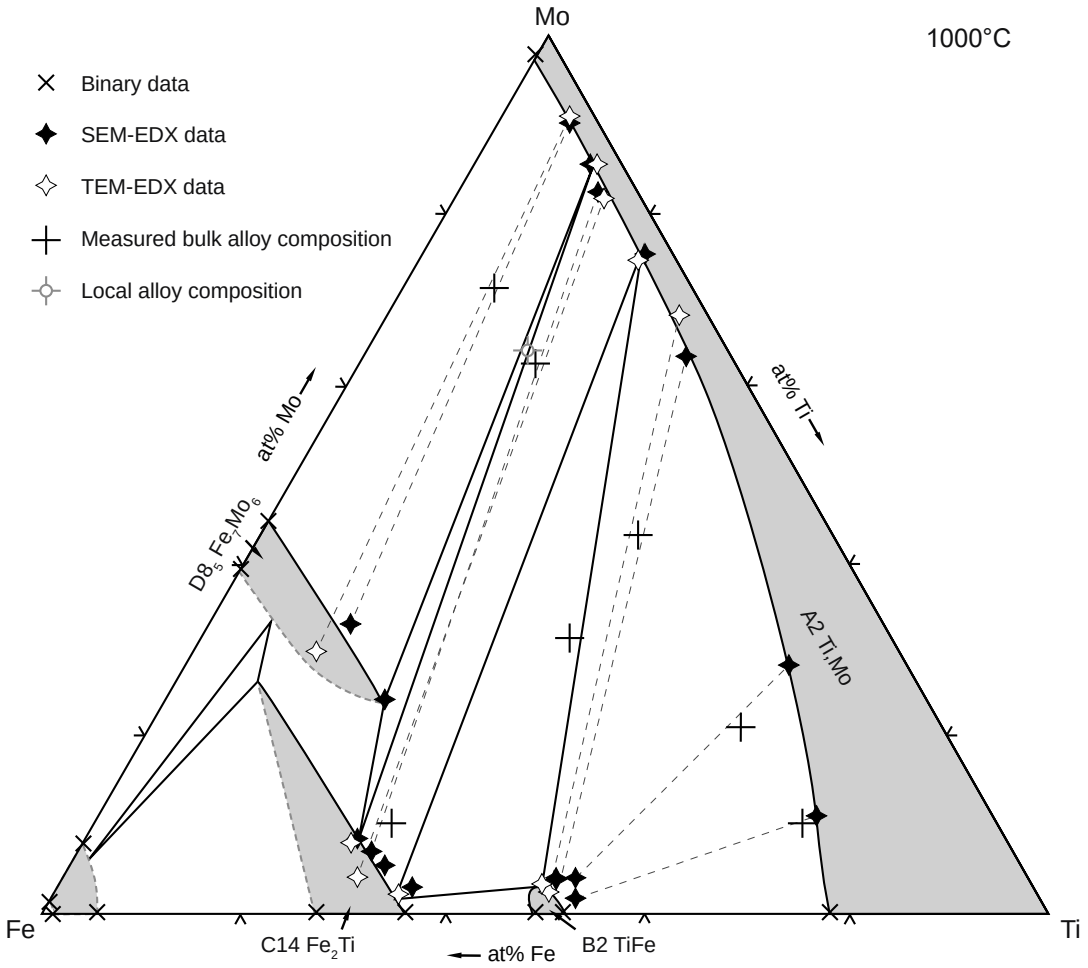

Figure 11 – Experimentally determined 1000°C isothermal section of the Fe-Mo-Ti ternary system.

Tables

Table 1 – Summary of the phases observed in the Fe-Mo, Fe-Ti and Mo-Ti binary phase diagrams including common phase designations and crystal structure data [21,22,25].

Phase	Strukturbericht	Pearson	Space group	Prototype	Composition	a (Å)	c (Å)	Reference
Beta	A2	cI2	I m -3 m	W	Mo	3.15	-	[25]
Beta	A2	cI2	I m -3 m	W	Ti	3.28	-	[22]
Beta	A2	cI2	I m -3 m	W	Fe	2.89	-	[25]
$Beta_0$	B2		P m -3 m	CsCl	TiFe	2.99	-	[22]
Mu	$D8_5$	hR39	R -3 m	Fe_7W_6	Fe_7Mo_6	4.75	25.72	[25]
Lambda	C14	hP12	P 6_3/m m c	Zn_2Mg	Fe_2Mo	4.76	7.77	[25]
Lambda	C14	hP12	P 6_3/m m c	Zn_2Mg	Fe_2Ti	4.80	7.78	[22]
R	-	hR159	R -3	$Co_5Cr_2Mo_3$	Fe_5Mo_3	10.96	19.35	[25]
Sigma	$D8_b$	tP30	P 4_2/m n m	FeMo	FeMo	9.22	4.81	[25]
Alpha	A3	hP2	P 6_3/m m c	Mg	Ti	2.95	4.67	[21]
Gamma	A1	cF4	F m -3 m	Cu	Fe	3.648	-	[25]

Table 2 – Alloy designations, nominal and average measured compositions for the alloy studied.

	Target composition			Nominal composition		
Alloy	Ti (at%)	Fe (at%)	Mo (at%)	Ti (at%)	Fe (at%)	Mo (at%)
TF20M10	70	20	10	70.2 ± 0.2	19.6 ± 0.2	10.2 ± 0.1
TF20M20	60	20	20	58.8 ± 0.5	20.0 ± 0.7	21.2 ± 0.8
TF20M40	40	20	40	37.6 ± 0.4	19.8 ± 0.3	42.6 ± 0.6
TF20M60	20	20	60	17.8 ± 0.3	19.4 ± 0.2	62.8 ± 0.3
TF20M70	10	20	70	9.7 ± 0.1	19.3 ± 1.5	70.9 ± 1.7
TF33M33	33.3	33.3	33.3	36.7 ± 0.8	31.7 ± 1.1	31.6 ± 0.4
TF60M10	30	60	10	29.7 ± 0.1	59.8 ± 0.1	10.5 ± 0.1

Table 3 – Phases identified in each alloy studied and their associated compositions.

Alloy	Phase	Technique	Ti (at%)	Fe (at%)	Mo (at%)	a (Å)	c (Å)
TF20M10	A2	SEM-EDX	71.4 ± 0.2	17.7 ± 0.1	10.8 ± 0.1	3.15	-
	B2	SEM-EDX	52.4 ± 0.2	45.7 ± 0.3	1.9 ± 0.1	3.00	-
TF20M20	A2	SEM-EDX	60.3 ± 0.4	11.5 ± 0.2	28.3 ± 0.4	3.17	-
	B2	SEM-EDX	51.4 ± 0.2	45.0 ± 0.2	3.6 ± 0.1	3.00	-
TF20M40	A2	SEM-EDX	32.1 ± 1.2	4.4 ± 0.4	63.5 ± 1.1	3.15	-
		STEM-EDX	29.2 ± 0.4	3.2 ± 0.2	67.6 ± 0.5	-	-
	B2	SEM-EDX	49.9 ± 0.3	46.8 ± 0.3	3.3 ± 0.1	2.99	-
		STEM-EDX	47.9 ± 0.5	49.1 ± 0.3	3.0 ± 0.3	-	-
TF20M60	A2	SEM-EDX	14.1 ± 2.2	3.4 ± 0.3	81.6 ± 2.3	3.15	-
		STEM-EDX	12.6 ± 0.7	1.9 ± 0.3	85.5 ± 0.9	-	-
	C14	SEM-EDX	29.2 ± 0.7	63.8 ± 1.6	7.0 ± 1.4	4.80	7.88
		STEM-EDX	26.3 ± 1.2	65.2 ± 2.8	8.5 ± 3.8	-	-
TF20M60	A2	SEM-EDX	12.1 ± 0.2	2.8 ± 0.3	85.1 ± 0.5	-	-
(local region)	C14	SEM-EDX	27.1 ± 0.3	64.4 ± 0.4	8.4 ± 0.2	-	-
	$D8_5$	SEM-EDX	22.0 ± 0.6	53.8 ± 0.7	24.2 ± 1.1	4.87	27.13
TF20M70	A2	SEM-EDX	7.8 ± 0.4	2.5 ± 0.7	89.7 ± 0.9	3.15	-
		STEM-EDX	7.3 ± 0.1	2.0 ± 0.1	90.7 ± 0.3	-	-
	$D8_5$	SEM-EDX	14.6 ± 0.8	52.9 ± 0.4	32.4 ± 1.0	4.84	26.95
		STEM-EDX	12.3 ± 0.4	58.1 ± 1.5	29.6 ± 1.4	-	-
TF60M10	C14	SEM-EDX	31.4 ± 0.2	63.4 ± 0.3	5.2 ± 0.4	4.81	7.91
		STEM-EDX	29.3 ± 0.7	66.3 ± 0.4	4.4 ± 1.0	-	-
	A2	SEM-EDX	24.1 ± 1.6	31.9 ± 6.8	44.1 ± 8.4	3.13	-
		STEM-EDX	15.2 ± 0.9	3.9 ± 0.6	81.0 ± 1.4	-	-
TF33M33	A2	SEM-EDX	22.1 ± 0.7	2.9 ± 0.4	75.0 ± 1.0	3.16	-
		STEM-EDX	22.1 ± 1.3	3.5 ± 0.2	74.5 ± 1.4	-	-
	B2	SEM-EDX	49.4 ± 0.9	46.8 ± 0.9	3.8 ± 0.5	2.99	-
		STEM-EDX	48.9 ± 0.4	48.8 ± 0.2	2.3 ± 0.4	-	-
	C14	SEM-EDX	35.2 ± 0.4	61.3 ± 0.5	3.5 ± 0.5	4.82	7.90
		STEM-EDX	34.3 ± 0.3	63.4 ± 0.5	2.3 ± 0.6	-	-